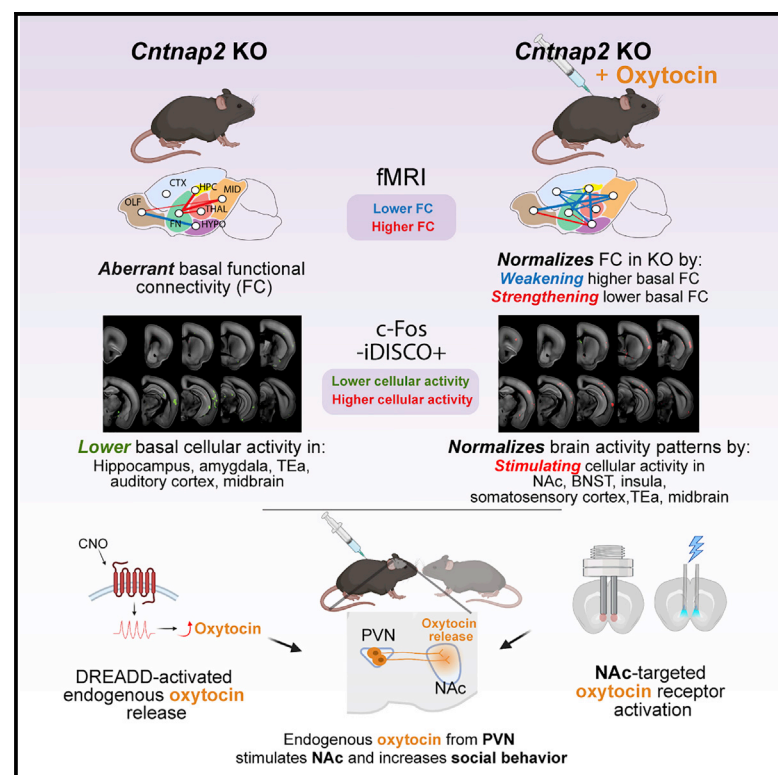


Oxytocin normalizes altered circuit connectivity for social rescue of the *Cntnap2* knockout mouse

Graphical abstract



Authors

Katrina Y. Choe,
Richard A.I. Bethlehem,
Martin Safrin, ..., Olga Peñagarikano,
Neil G. Harris, Daniel H. Geschwind

Correspondence

choek@mcmaster.ca (K.Y.C.),
dhg@mednet.ucla.edu (D.H.G.)

In brief

Using fMRI and c-Fos-iDISCO+, Choe et al. show that mice missing *Cntnap2*, an ASD-linked gene, exhibit altered functional brain connectivity. This is normalized by exogenous oxytocin, which also rescues social deficits. Critical to this process is endogenous oxytocin signaling within the NAc, implicating its potential role in ASD-associated social impairments.

Highlights

- We integrate brain-wide c-Fos-iDISCO+ imaging and fMRI in an ASD mouse model
- Overlapping activity and connectivity profiles reveal disrupted brain networks
- Oxytocin strongly activates KO brain to normalize functional connectivity patterns
- We identify nucleus accumbens as a key hub for OXT modulation of KO social behavior

Article

Oxytocin normalizes altered circuit connectivity for social rescue of the *Cntnap2* knockout mouse

Katrina Y. Choe,^{1,2,3,*} Richard A.I. Bethlehem,⁴ Martin Safrin,¹ Hongmei Dong,¹ Elena Salman,¹ Ying Li,¹ Valery Grinevich,⁵ Peyman Golshani,^{1,2,6} Laura A. DeNardo,⁸ Olga Peñagarikano,⁹ Neil G. Harris,¹⁰ and Daniel H. Geschwind^{1,2,6,7,11,*}

¹Department of Psychiatry and Biobehavioral Sciences, Semel Institute, David Geffen School of Medicine, UCLA, Los Angeles, CA 90095, USA

²Center for Autism Research and Treatment, Semel Institute, David Geffen School of Medicine, UCLA, Los Angeles, CA 90095, USA

³Department of Psychology, Neuroscience & Behaviour, McMaster University, Hamilton, ON L8S 4K1, Canada

⁴Autism Research Centre, Department of Psychiatry, University of Cambridge, Cambridge CB2 0SZ, UK

⁵Department of Neuropeptide Research for Psychiatry, Central Institute of Mental Health, University of Heidelberg, Mannheim 68159, Germany

⁶Department of Neurology, David Geffen School of Medicine, UCLA, Los Angeles, CA 90095, USA

⁷Department of Human Genetics, David Geffen School of Medicine, UCLA, Los Angeles, CA 90095, USA

⁸Department of Physiology, David Geffen School of Medicine, UCLA, Los Angeles, CA 90095, USA

⁹Department of Pharmacology, School of Medicine, University of the Basque Country (UPV/EHU), Vizcaya 48940, Spain

¹⁰Department of Neurosurgery, David Geffen School of Medicine, UCLA, Los Angeles, CA 90095, USA

¹¹Lead contact

*Correspondence: choek@mcmaster.ca (K.Y.C.), dhg@mednet.ucla.edu (D.H.G.)

<https://doi.org/10.1016/j.neuron.2021.11.031>

SUMMARY

The neural basis of abnormal social behavior in autism spectrum disorders (ASDs) remains incompletely understood. Here we used two complementary but independent brain-wide mapping approaches, mouse resting-state fMRI and c-Fos-iDISCO+ imaging, to construct brain-wide activity and connectivity maps of the *Cntnap2* knockout (KO) mouse model of ASD. At the macroscale level, we detected reduced functional coupling across social brain regions despite general patterns of hyperconnectivity across major brain structures. Oxytocin administration, which rescues social deficits in KO mice, strongly stimulated many brain areas and normalized connectivity patterns. Notably, chemogenetically triggered release of endogenous oxytocin strongly stimulated the nucleus accumbens (NAc), a forebrain nucleus implicated in social reward. Furthermore, NAc-targeted approaches to activate local oxytocin receptors sufficiently rescued their social deficits. Our findings establish circuit- and systems-level mechanisms of social deficits in *Cntnap2* KO mice and reveal the NAc as a region that can be modulated by oxytocin to promote social interactions.

INTRODUCTION

Social deficits are at the core of autism spectrum disorder (ASD), a neurodevelopmental disorder with rapidly rising prevalence (Baio et al., 2018; Kogan et al., 2018). Efforts to develop more effective treatments are hindered by our limited understanding of the neural basis of social behavior and its disruption in ASD (Barak and Feng, 2016; Chadman, 2014; Ghosh et al., 2013). Several decades of research have revealed the complex and context-dependent nature of social behavior and how it is influenced by neuromodulators such as oxytocin (OXT; Anderson, 2016; Insel, 2010; Meyer-Lindenberg et al., 2011; Mitre et al., 2018; Stanley and Adolphs, 2013; Steinman et al., 2019). Although several brain regions have been identified as playing key roles in social behavior (Chen and Hong, 2018; Kim et al., 2015; Ko, 2017; Lebow and Chen, 2016; Walum and Young, 2018), it is not known how individual components interact to generate neurotypical social behavior and how such interactions are altered in ASD. Furthermore, abnormal func-

tional connectivity has been variably identified in ASD using resting-state functional MRI (rsfMRI) (Di Martino et al., 2014; Hull et al., 2017; King et al., 2019), but there is no consensus as to which specific abnormalities are linked to social deficits. A possible contributing factor is the heterogeneous genetic architecture of ASD (Jeste and Geschwind, 2014; Takumi et al., 2020). Indeed, emerging observations support the notion that genetic heterogeneity contributes substantially to clinical heterogeneity as evidenced by characteristic phenotypes associated with specific mutations (Bernier et al., 2014; DiMario et al., 2015; de la Torre-Ubieta et al., 2016; Hagerman et al., 2017; Ruzzo et al., 2019). To advance our understanding of the mechanisms behind social deficits in ASD, a reasonable approach is to map circuit phenotypes associated with a specific ASD-risk gene mutation using monogenic *in vivo* models of ASD, offsetting the challenges imposed by ASD's genetic heterogeneity.

We previously reported social deficits in mice harboring mutations in the Contactin-associated protein-like 2 gene (*CNTNAP2*;

Peñagarikano et al., 2011, 2015), in which loss-of-function recessive mutations cause a syndromic form of ASD (Strauss et al., 2006). This mouse knockout model (*Cntnap2*^{-/-} or *Cntnap2* KO) has been established as a robust model for studying the neurobiological mechanisms of ASD (Brumback et al., 2018; Levy et al., 2019; Peñagarikano et al., 2011; Scott et al., 2019; Selimbeyoglu et al., 2017). A prominent feature of the KO mouse is a dysfunctional central OXT system that appears to be linked with its social deficits. *Cntnap2* is strongly expressed in OXT neurons, and deleting *Cntnap2* in mice reduces the total amount of brain OXT and the number of OXT-immunoreactive neurons in the paraventricular nucleus (PVN) of the hypothalamus (Peñagarikano et al., 2015). Remarkably, either exogenous supplementation of OXT or activation of endogenous OXT release via chemogenetic or pharmacological strategies temporarily normalizes the social impairment (Peñagarikano et al., 2015). Recently, defects in the OXT system have also been linked to several other monogenic forms of ASD (Harony-Nicolas et al., 2017; Hörnberg et al., 2020; Kitagawa et al., 2021; Lewis et al., 2020), further highlighting its role in ASD-related social functioning.

Here, we performed extensive circuit mapping in the *Cntnap2* KO by integrating, for the first time, two methods that allow brain-wide mapping of neuronal activity: high-field mouse fMRI (Ahrens and Dubowitz, 2001; Grandjean et al., 2020) and lightsheet imaging of c-Fos expression in iDISCO+-cleared brains (c-Fos-iDISCO+; DeNardo et al., 2019; Renier et al., 2016). We identified evidence of dysregulated resting-state functional connectivity (rsFC) in KO mice at the macroscale level and across a key set of social brain regions and their connectivity relationship to the rest of the brain. Exogenously administered OXT either partially or fully reversed these aberrant patterns of connectivity in KO mice by activating a variety of brain areas in a manner positively correlated with the density of OXT fiber projections. The nucleus accumbens (NAc) was strongly activated by experimentally stimulated release of endogenous OXT in KO mice, consistent with its emergent role as a hub in the “social salience and reward network” (Dölen et al., 2013; Johnson et al., 2017). To directly test the contribution of OXT in the NAc in the social impairment and rescue in KO mice, we induced either pharmacological or optogenetic activation of OXT signaling in the NAc and found that either treatment sufficiently increased social behavior. These results are the first to demonstrate brain-wide functional network abnormalities related to social deficits, as well as their restoration by OXT in a genetic model of ASD that exhibits construct, face, and predictive validity to the human condition (Peñagarikano et al., 2011, 2015).

RESULTS

Exogenous OXT rescues aberrant functional connectivity in KO mice

Because individuals with ASD commonly exhibit abnormal patterns of rsFC (Hahamy et al., 2015; Hull et al., 2017; Lau et al., 2019; Lawrence et al., 2019; Takumi et al., 2020), we asked whether we could also find aberrant rsFC in *Cntnap2* KO mice and whether OXT could rescue it. We acquired blood-oxygen-level-dependent (BOLD)-weighted rsfMRI data from dexmedetomidine-sedated wild-type (WT) and KO mice prior to and post OXT administration (intraperitoneal [i.p.], 1 mg/kg) and computed rsFC (STAR Methods; Figure S1). We compared the average rsFC between seven major brain structures classified according to the Allen Mouse Brain Atlas (Lein et al., 2007; Wang et al., 2020), namely the olfactory (OLF), isocortex (CTX), hippocampus (HPC), forebrain nuclei (FN), thalamus (TH), hypothalamus (HYPO), and midbrain (MID). We identified five pairs of connections that exhibited distinct macroscale rsFC in KO mice, four of which were stronger (in the order of decreasing statistical significance: FN-HPC, FN-TH, FN-MID, and OLF-MID) and only one of which was weaker (OLF-HYPO; $p < 0.01$; Figure 1A). These results demonstrate profound rsFC differences in KO mice at the macroscale level, centered on the FN.

Because KO mice display deficits in social behavior (Peñagarikano et al., 2011, 2015), we next examined whether they also exhibit specific rsFC impairments in brain regions established to play important roles in mouse social behavior (e.g., medial prefrontal cortex (mPFC), olfactory brain regions, NAc, bed nucleus of stria terminalis (BNST), septal regions, hypothalamus; see STAR Methods for entire list; Figure 1B; Chen and Hong, 2018; Kim et al., 2015; Ko, 2017; Lebow and Chen, 2016). The average rsFC across these key social regions was significantly lower in *Cntnap2* KO mice relative to WT ($p = 0.01$; Figures 1B and S2B). In contrast, the average rsFC between this group of key social regions and the rest of the brain (e.g., thalamus, sensory cortices, brainstem; subsequently referenced as “other” regions) was significantly higher in KO mice ($p < 0.001$). No significant difference was observed between WT and KO mice when we compared average rsFC across the “other” regions ($p = 0.74$), indicating that genotype differences in rsFC may be specific to connections shared with social regions. Taken together, these data show that KO mice display a specific impairment in rsFC involving key social areas, manifesting as weaker connectivity within this group of functionally linked brain regions and stronger connectivity between these and the rest of the brain.

Notably, i.p. OXT had a much stronger impact on the macroscale rsFC on KO mice compared to WT controls. In WT, OXT significantly attenuated the rsFC between five pairs of macroscale connections (OLF-CTX, CTX-FN, FN-HPC, CTX-HYPO, and OLF-HYPO; $p < 0.01$; Figure 1C). In KO mice, a higher number of macroscale connections were modified by OXT—these include rsFC attenuation in eight pairs of connections (FN-HPC, OLF-MID, HPC-HYPO, FN-MID, CTX-TH, CTX-MID, CTX-HPC, and CTX-HYPO) and increase in two pairs (FN-HYPO and OLF-HYPO; $p < 0.01$; Figure 1D). These changes to rsFC were sufficient for partially rescuing the basal connectivity phenotype of KO mice, as reported above. To identify specific brain areas that are the most likely to serve as a connectivity “hub” for the effect of OXT on rsFC, we established a ranked list of the top ten strengthened and top ten weakened region of interest (ROI) pairs after OXT administration for each of the WT and KO datasets, then identified which individual regions appeared most frequently in this list. In WT mice, the motor cortex (MOT), infralimbic and prelimbic cortex (LIM), anterior cingulate cortex (ACC), and the lateral septum (LS) were identified as top regions in the list. In KO mice, the NAc, BNST, medial septum

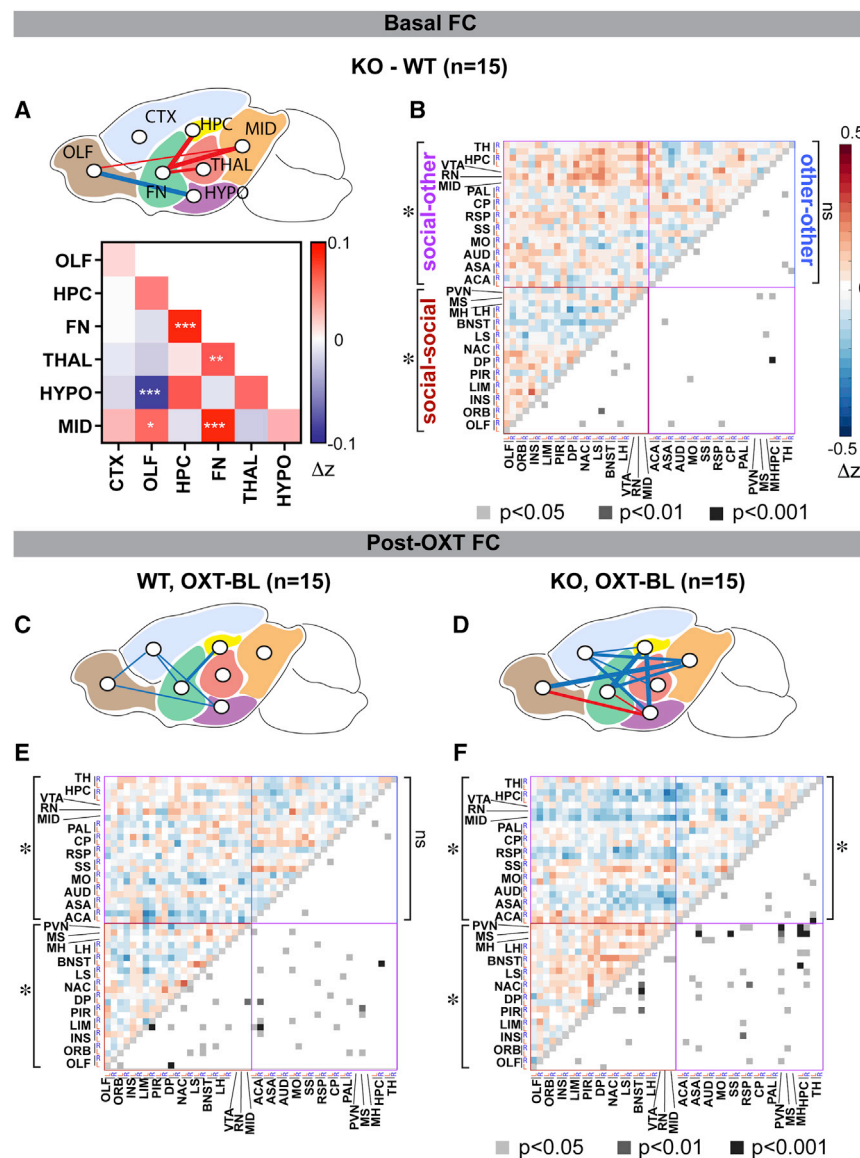


Figure 1. Structure- and function-based comparisons of functional connectivity between WT and KO mice before and after OXT

(A) Top: macroscale comparison of basal rsFC between WT and KO mice (KO-WT) in pairs of seven major brain structures (OLF, olfactory cortex; CTX, isocortex; FN, forebrain nuclei; HPC, hippocampus; THAL, thalamus; HYPO, hypothalamus; MID, midbrain). Lines indicate significant WT-KO rsFC differences ($p < 0.01$, Monte Carlo permutation test). Line thickness indicates higher statistical significance. Red, WT < KO; blue, KO < WT. * $p < 0.01$, ** $p < 0.005$, *** $p < 0.001$. Bottom: heatmap represents rsFC differences (red-blue, Δz) for each pair.

(B) Heatmaps representing basal WT-KO rsFC differences (upper triangle, red-blue) and p values (lower triangle, grayscale; unpaired t test, uncorrected values) for each pair. Colored boxes indicate pairwise rsFC of social-social (red), social-other (purple), and other-other (blue) regions (Monte Carlo permutation test).

(C and D) Macroscale rsFC shifts triggered by i.p. OXT injection compared to baseline (OXT-BL; $t = 30$ min) for WT (C) and KO (D) mice.

(E and F) Heatmaps representing OXT-induced rsFC changes (upper triangle, red-blue) and p values (lower triangle, grayscale; paired t test, uncorrected values) for each ROI pair in WT (E) and KO (F) mice. * $p < 0.05$; ns, not significant.

(MS), and the HPC were identified as the top regions (Table S1). Notably, three of these four top regions in KO mice belong to the FN, which exhibited the highest number of aberrant macroscale connections prior to OXT application, as noted above. Furthermore, these four top regions belong to the previously proposed “social decision-making network” (O’Connell and Hofmann, 2012) and align with the currently hypothesized mechanism of social facilitation by OXT—strengthening the connectivity across a network of brain areas involved in social functions (Johnson and Young, 2017).

To further understand the effect of OXT on these connectivity hub regions in KO mice, we examined the time course of OXT-induced rsFC shifts in two ROI pairs featuring the four connectivity hub regions, NAc-BNST and MS-HPC. These connections showed a robust and progressive change in rsFC in response to OXT administration in KO mice ($p < 0.05$; Figure S2C). No sig-

nificant change in rsFC was detected in either WT mice receiving OXT or KO mice receiving saline (SAL; $p > 0.05$), consistent with the previously reported absence of OXT augmentation of social behavior in WT mice (Peñagarikano et al., 2015). Finally, we examined whether OXT normalized the basal rsFC phenotypes observed across social regions in KO mice. We found that OXT elevated rsFC across these social regions and concomitantly reduced rsFC between social and other regions, normalizing the basal connectivity phenotypes in KO mice ($p < 0.001$; Figures 1E, 1F, and S2B).

Atlas-based connectivity analysis averages signals within pre-determined ROIs based on atlas parcellation and therefore can mask sub-regional effects. To overcome this limitation, we next computed pairwise rsFC across 40 ROIs defined by data-driven independent component analysis (ICA; Smith et al., 2013), which decomposes imaging data into independent spatial maps and associated time courses (Beckmann and Smith, 2004). In agreement with the atlas-based connectivity analysis, OXT administration appeared to specifically modulate the KO brain, significantly shifting the rsFC between three pairs of independent components (ICs) in KO mice, but none in WT (Figures 2A–2C; false discovery rate [FDR] < 0.1). Two were reduced: IC1 (centered around the visual cortex)-IC3 (lateral hypothalamus) and IC11 (anterior cingulate cortex)-IC31 (dorsal

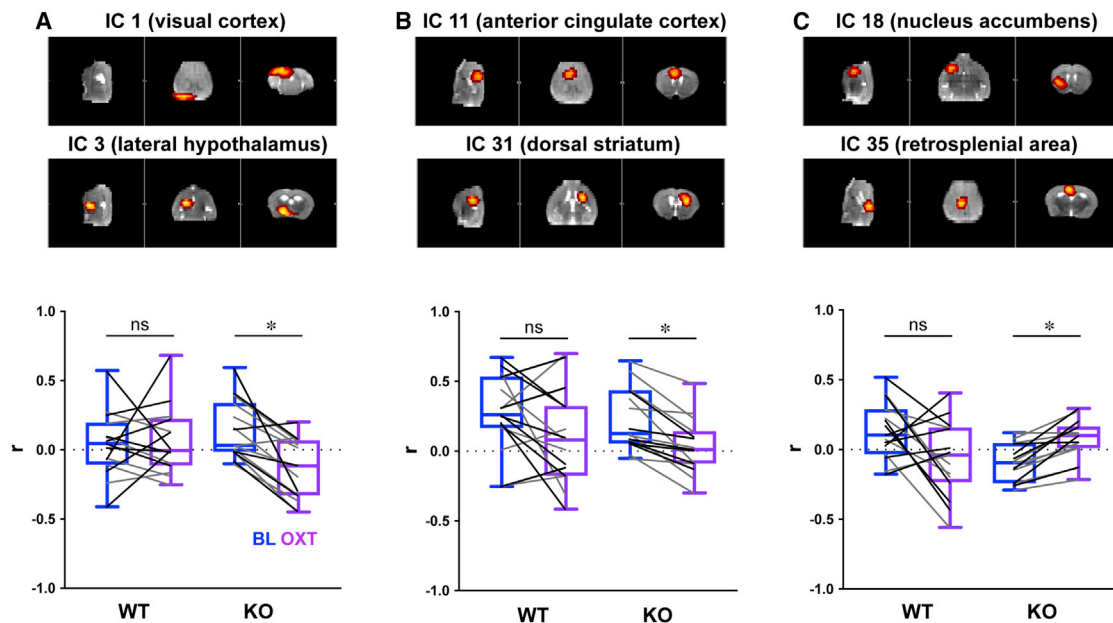


Figure 2. Independent component analysis of functional connectivity between WT and KO mice before and after OXT
(A–C) (A) IC1–IC3; (B) IC11–IC31; (C), IC18–IC35. Box-whisker plots represent a summary of R values (whisker: min–max values, box: 25th–75th percentiles, lines: individual before–after values, black for males and gray for females) of between-component connectivity for each genotype group, before and after OXT ($t = 30$ min). Out of 40 identified ICs, OXT significantly modified rsFC between three KO IC pairs and no WT pairs (paired t test, $^*FDR < 0.1$).

striatum), both of which represent connections between “social” and “other” areas. Therefore, these results are in accordance with our atlas-based ROI pairwise connectivity comparisons in which OXT reduces the overall rsFC between the two groups. In contrast, OXT increased the relative rsFC between IC18 (ventral striatum/NAc) and IC35 (retrosplenial area) despite our classification of this connection as being between “social” and “other” regions. Both brain regions are of special interest—the retrosplenial area is a component of the default mode network (DMN), a group of midline cortical regions whose activity is correlated at rest in humans (Raichle, 2015) and mice (Stafford et al., 2014). Interestingly, the rsFC between the retrosplenial cortex and the rest of the DMN is impaired in ASD (Starck et al., 2013) and correlated with social symptom severity in humans (Lynch et al., 2013) and in *Cntnap2* KO mice (Liska et al., 2018).

Together, these rsfMRI data suggest that KO mice exhibit aberrant rsFC at the macroscale and individual circuit levels, largely reversed after OXT administration. These data also highlight the potential importance of several FN, specifically NAc, BNST, and septal areas, whose rsFC with other brain regions is robustly modified after OXT administration in KO mice. Their well-known contributions to social behavior (Anderson, 2016; Chen and Hong, 2018; Kim et al., 2015) as core components of social salience and reward networks (Johnson and Young, 2017) suggest that these regions play key roles in the pro-social effect of OXT in KO mice.

Exogenous OXT robustly increases the BOLD signal in the KO mouse brain

The above data indicate that OXT strongly modifies rsFC across the KO brain to closely resemble WT patterns while having a

negligible effect on the WT brain. We next examined whether a disparity in OXT-triggered brain activity could underlie these differences, hypothesizing that OXT would strongly modulate the brain activity of KO mice while having a limited effect on WT mice (Peñagarikano et al., 2015). To test this, we measured brain-wide changes in activity triggered by OXT administration in WT and KO mice using pharmacological MRI (phMRI; Leslie and James, 2000). In line with previous findings (Galbusera et al., 2017), peripherally administered OXT failed to increase the relative amplitude of the BOLD signal in any brain region of WT mice (versus SAL-injected WT mice; Figure 3A; see Figures S1B and S3A for acquisition and analysis schematics). In contrast, OXT administration robustly increased the relative BOLD signal amplitude across numerous brain regions in KO mice (versus SAL-injected KO mice; Figures 3A and S3B). Significant negative BOLD fluctuations were observed in WT mice injected with OXT; however, they were not statistically different from responses to SAL injections (Figure S3C). These results suggest that the observed stimulatory effect of OXT on brain activity is unique to KO mice, which parallels the KO-restricted behavioral effects of OXT (Peñagarikano et al., 2015).

The PVN showed the strongest increase in BOLD signal compared with other regions, raising the possibility that exogenously administered OXT was triggering the release of its endogenous form (Figure S3B). Robust activation by OXT was also detected in several regions with established roles in social behavior, including the lateral and medial hypothalamus (Anderson, 2016), the BNST (Lebow and Chen, 2016), and the dorsal peduncular area, a sub-region of the mPFC (Riga et al., 2014; Figures 3A and S3B). Outside of these key social regions, OXT also activated various other cortical (e.g., somatosensory, motor,

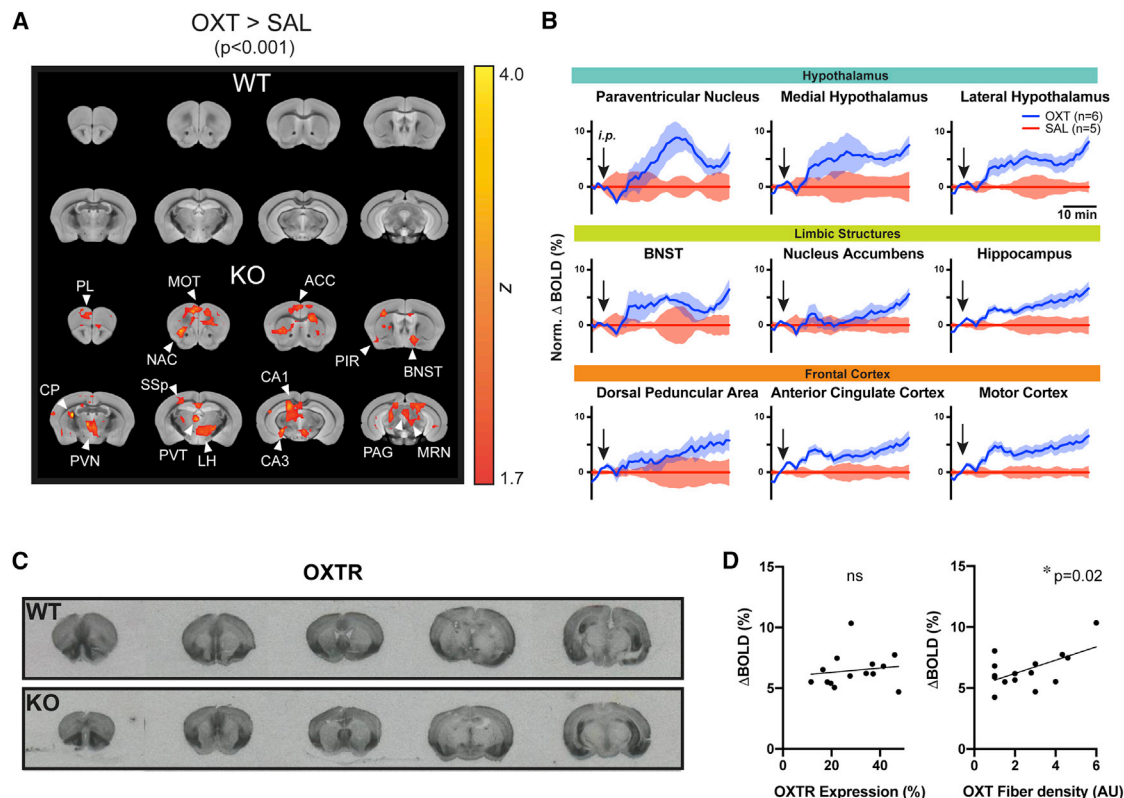


Figure 3. Exogenous OXT induces a selective pattern of BOLD signal increases in the KO mouse

(A) Red-orange blobs overlaid on a reference structural scan indicate significantly activated voxels (OXT > SAL). $n = 5$ –6/group.

(B) Time plots compare percent BOLD signal change induced by OXT or SAL in selected brain regions.

(C) OXTR autoradiography images reveal a relatively preserved pattern of OXTR expression in KO, with the exception of the lateral septum.

(D) Scatterplots and regression lines compare correlations between average percent BOLD change by OXT and OXTR expression density (left) or OXT fiber density (right) in each examined ROI (circle). $*p < 0.05$; ns, not significant.

and retrosplenial cortex) and subcortical (e.g., hippocampus, thalamus, midbrain [including the ventral tegmental area]) regions. These align with the previously reported ability of OXT to influence the excitability of social and other brain regions, including the PVN (Inenaga and Yamashita, 1986), mPFC (Nakajima et al., 2014), hippocampus (Owen et al., 2013), auditory cortex (Marlin et al., 2015), and olfactory cortex (Oettl et al., 2016).

We next compared the dynamics of BOLD signal fluctuations in brain regions exhibiting the strongest degree of activation by OXT, including hypothalamic, limbic, and frontal cortical areas (Figure 3B). As mentioned above, the PVN displayed the strongest BOLD activation, having a peak response at $\sim 8\%$ above baseline at $t = \sim 20$ min post injection, followed by a reduced but sustained level throughout the rest of the scan period ($t = \sim 40$ min post injection). Other hypothalamic areas (e.g., medial and lateral hypothalamus) and limbic structures (e.g., BNST, NAc, hippocampus, and dorsal peduncular area) lacked the peak response but still maintained a sustained pattern of BOLD increase. Other cortical areas, including the anterior cingulate cortex and motor cortex, showed a mixed response, composed of an initial peak followed by a sustained response. Together, these results suggest that OXT injection in KO mice stimulates several brain regions, many of which have previously been identified as critical for social function (John-

son and Young, 2017). The BOLD activation kinetics in these regions are in line with the behavioral time course of administered OXT identified in published studies (~ 20 min post i.p. administration; Peñagarikano et al., 2015).

Given the robust and region-specific pHMRI activation of the KO brain by OXT, we explored whether differences in OXT receptor (OXTR) expression could account for these effects by comparing OXTR expression between WT and KO mouse brains with receptor autoradiography. KO mice exhibited a largely similar pattern of brain-wide OXTR binding to WT (Figure 3C). The highest binding densities in both groups were observed in the olfactory areas, including the piriform cortex, anterior olfactory nuclei, and taenia tecta; various cortical areas including the mPFC, somatosensory, auditory, association and motor cortex; hippocampal CA3; hypothalamus; and the amygdala, similar to previously reported findings in WT mice (Gigliucci et al., 2014; Hammock and Levitt, 2013). One notable exception to the typical expression pattern was found in the dorsal region of the lateral septum, where the binding density in KO mice appeared to be higher than that in WT mice (Figure S3D). This is particularly interesting in light of work in voles, in which a high level of OXTR expression in this region has been positively correlated with an inability to form social pair bonds (Insel and Shapiro, 1992).

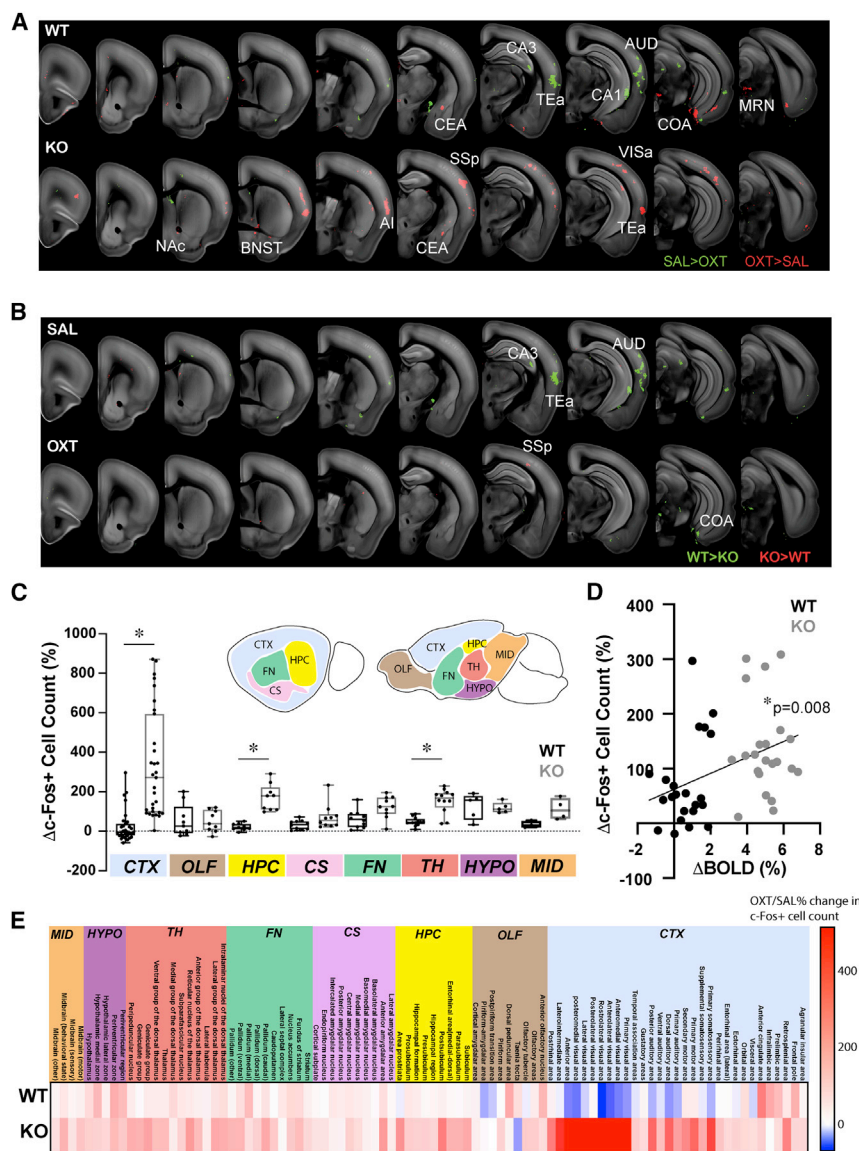


Figure 4. Exogenous OXT induces an overlapping change in brain-wide c-Fos and BOLD activity

(A and B) Within-genotype (A) and between-genotype (B) comparisons of regional activity levels between OXT- and SAL-injected mice using c-Fos-iDISCO+. Red (OXT > SAL or KO > WT) and green (SAL > OXT or WT < KO) blobs overlaid on the reference brain image indicate voxels with significantly different ($p < 0.005$) c-Fos+ cell counts.

(C) Bar-whisker plots (whisker: min–max values, box: 25th–75th percentiles, circles: individual ROI values) compare the average percent change in c-Fos+ cell counts between WT (black) and KO (gray) mice. Kruskal-Wallis test.

(D) Significant correlation between OXT-induced regional activity changes measured by pHMRI (x axis) and iDISCO+ (y axis) indicated by a regression line.

(E) Heatmap illustrating WT versus KO regional percent changes to c-Fos+ cell count after OXT. Circles, individual ROI average values. $n = 4$ –5/group. * $p < 0.05$.

iDISCO+-based brain-wide activity mapping confirms OXT activation patterns

To obtain a brain-wide activity map at a higher cellular resolution and without potentially interfering sedation effects in fMRI (Fukuda et al., 2013; Hablitz et al., 2019), we performed lightsheet imaging of the immediate early gene product c-Fos (a proxy marker of cellular activity; Gallo et al., 2018) in iDISCO+-cleared brains (DeNardo et al., 2019; Renier et al., 2016) and examined whether these data corresponded to the fMRI results. In agreement with the pHMRI results (Figure 3), OXT had an overwhelmingly stimulatory effect on the KO brain (versus SAL), increasing the number of c-Fos+ cells in many areas important for sensory and social functions including the NAc, BNST, anterior insula, somatosensory cortex, visual cortex, and the temporal association area ($p < 0.005$; Figure 4A). Also concordant with our pHMRI results, OXT had an overall inhibitory effect on WT brain activity (versus SAL), significantly reducing the number of c-Fos+ cells in regions including the CA1 and CA3 of the hippocampus, as well as a few cortical regions including temporal association cortex (TEa) and auditory cortex (AUD; $p < 0.005$; Figure 4A). A notable difference between the fMRI and c-Fos-iDISCO+ datasets was the strong activation of sensory cortical areas in KO mice, especially the somatosensory cortex and visual cortex, which were identified as two of the most significantly activated regions by c-Fos-iDISCO+ ($p < 0.005$; Figures S4A–S4D). These disparities may be due to amplification of the strong modulatory effects of OXT in these regions uncovered by the lack of sedation in these animals (e.g., Feng et al., 2018). These polarizing effects of OXT largely

To test whether OXTR expression patterns were implicated in the robust BOLD signal increases in KO mice after OXT administration, we examined whether a regional correlation exists between the amount of OXT-induced BOLD signal change in KO mice and the previously reported density of brain-wide OXTR expression in WT mice (Mitre et al., 2016). This analysis revealed no significant correlation between the two parameters ($r^2 = 0.02$; $p = 0.63$; linear regression analysis; Figure 3D; Table S2). Next, we explored whether the BOLD signal increases were related to the density of central OXT projections instead (Liao et al., 2020), finding a significant correlation ($r^2 = 0.33$; $p = 0.02$; linear regression analysis; Figure 3D; Table S2) between the 2 parameters. This supported the possibility of exogenous OXT administration triggering secretion of its endogenous form by PVN OXT neurons through their centrally projecting fibers that terminate in an array of downstream brain regions.

To test whether OXTR expression patterns were implicated in the robust BOLD signal increases in KO mice after OXT administration, we examined whether a regional correlation exists between the amount of OXT-induced BOLD signal change in KO mice and the previously reported density of brain-wide OXTR expression in WT mice (Mitre et al., 2016). This analysis revealed no significant correlation between the two parameters ($r^2 = 0.02$; $p = 0.63$; linear regression analysis; Figure 3D; Table S2). Next, we explored whether the BOLD signal increases were related to the density of central OXT projections instead (Liao et al., 2020), finding a significant correlation ($r^2 = 0.33$; $p = 0.02$; linear regression analysis; Figure 3D; Table S2) between the 2 parameters. This supported the possibility of exogenous OXT administration triggering secretion of its endogenous form by PVN OXT neurons through their centrally projecting fibers that terminate in an array of downstream brain regions.

minimized the baseline activity differences between WT and KO mice observed in SAL controls (Figure 4B), in strong agreement with our rsfMRI observations (Figure 1).

We next examined whether these distinct brain activity patterns elicited by OXT in KO mice were localized to any specific brain structures or their subregions by performing an atlas-based analysis. Then, we compared the percent change in c-Fos+ cell count for each of the six major brain structures as identified above, plus the cortical subplate (CS), another major brain structure that could not be investigated via fMRI because of a loss of signal from geometric distortions common in echo planar imaging (Febo, 2011). As in our voxel-wise analyses, brain regions classified as part of the CTX ($p < 0.0001$), HPC ($p = 0.002$), and TH ($p = 0.045$) were more strongly activated in KO mice compared to WT (Figures 4C and 4E). To directly test whether the iDISCO+ brain activity mapping results reliably validate the robust opposing effect of OXT in WT versus KO mice observed with phMRI (Figure 3), we identified 22 ROIs present in both datasets and plotted the percent activation against each other (STAR Methods; Table S3). This analysis confirmed that, despite measuring remarkably diverse features representing brain activity at different scales in different cohorts of mice, the two brain-wide datasets are indeed significantly correlated ($r^2 = 0.16$; $p = 0.008$; Figure 4D). Moreover, the iDISCO+ results also validated the phMRI data on a regional basis—out of the 13 brain regions identified as having the highest degree of OXT-induced activation within the phMRI dataset, five regions also showed significant OXT-mediated increases in c-Fos+ cell counts with iDISCO+ brain activity mapping analysis (FDR < 0.1; Figures S4A–S4C). This group of OXT-activated brain regions was composed of several social and motor-sensory regions, including the BNST, primary and secondary somatosensory cortex, primary motor cortex, and the anterior visual area. In summary, these iDISCO+ results reveal robust activation of social and sensory regions by OXT in KO mice, resulting in a normalization of aberrant activity patterns in these mice. Taken together, these observations provide independent confirmation of the fMRI results at a cellular level, highlighting the complementarity of these two powerful brain-mapping approaches.

DREADD stimulation of endogenous OXT release strongly activates KO NAC

Having established with three separate methods (i.e., phMRI, rsfMRI, c-Fos-iDISCO+) that OXT specifically impacts brain activity and functional connectivity in KO mice, including a network of key social areas, we asked to what extent these results were a consequence of the central activity of OXT versus its potential indirect effects through peripheral receptors (Qin et al., 2009; Quintana et al., 2015). To isolate the central component of the OXT-mediated effects observed in KO mice, we used the designer receptors exclusively activated by designer drug (DREADD) approach specifically targeted to PVN OXT neurons (AAV-OXT-hM3D(Gq)-mCherry or AAV-hSyn-DIO-hM3D(Gq)-mCherry in heterozygous Oxt-Cre mice; Fields et al., 2012; Grund et al., 2019; Krashes et al., 2011; Peñagarikano et al., 2015; Tang et al., 2020; Figure 5A). We chemogenetically stimulated the activity of these neurons

in a group of WT and KO mice to trigger endogenous delivery of OXT via its natural axon projections throughout the brain (Knobloch et al., 2012). Another group of mice received AAV-mOXT-Venus (without the construct for hM3D(Gq), the DREADD receptor) or AAV-hSyn-DIO-mCherry injections into the PVN to serve as controls. Using immunohistochemistry and confocal imaging, we established c-Fos+ cell counts in the PVN and several forebrain areas (NAc, BNST, lateral septum, mPFC, and basolateral amygdala), regions selected based on their strong modulation of activity and rsFC by exogenous OXT in KO mice (Figures 1, 2, 3, and 4).

As a proof-of-principle experiment, we first examined the effect of the DREADD treatment in the PVN and, as expected, observed in both WT and KO mice a large (~5-fold) increase in the number of c-Fos+ cells following delivery of the DREADD agonist at a dose that rescues social behavior in KO mice (5 mg/kg i.p. Clozapine-n-oxide; Figures 5B and 5C; Table S4; Peñagarikano et al., 2015). We next examined c-Fos+ cell counts in other regions of interest. Notably, the NAc in KO mice showed a significant DREADD-mediated increase in the number of c-Fos+ cells ($p = 0.008$; Figures 5D and 5E; Table S4). This effect was absent in WT NAc after DREADD treatment ($p = 0.75$). Additionally, there was a near-significant basal difference in c-Fos+ cell counts between WT and KO mice in the BNST ($p = 0.08$), suggesting its potential abnormal activity in the KO brain. In contrast, the lateral septum and BNST, other FN areas that we earlier identified as being activated by i.p. OXT (Figures 3 and 4; Table S4), did not exhibit significant activation increases following chemogenetically stimulated endogenous OXT release (Figure S5). The mPFC and basolateral amygdala, two other brain areas well established to play central roles in social behavior (Ko, 2017; Selimbeyoglu et al., 2017; Yang and Wang, 2017), but which receive sparse OXT fiber projections (Liao et al., 2020), also did not show any increase in c-Fos+ cell counts in KO mice in after DREADD activation (Figure S5; Table S5). These results suggested to us that the NAc was the most likely region to mediate the previously demonstrated pro-social behavior in KO mice elicited by chemogenetic activation of PVN OXT neurons (Peñagarikano et al., 2015). This is consistent with the known role of the NAc as a hub in social reward (Clithero et al., 2011; Kohls et al., 2013; Spreckelmeyer et al., 2009; Vanderschuren et al., 2016) and its involvement in ASD-related social deficits based on data from humans (Scott-Van Zeeland et al., 2010; Supekar et al., 2018; van Rooij et al., 2018) and other ASD mouse models based on human genetic evidence (Karayannis et al., 2014; Walsh et al., 2018).

Experimental enhancement of NAC OXT signaling sufficiently increases social behavior in KO mice

To directly examine the functional contribution of OXT signaling in the NAc to the pro-social effect of OXT in KO mice *in vivo*, we performed a home cage reciprocal social interaction assay in mice after a bilateral microinjection of TGOT (a selective OXTR agonist; Eliava et al., 2016; Lowbridge et al., 1977) into the NAc through an implanted cannula (Figures 6A, 6B, and S6A). Although both NAc core and shell areas have been implicated in social reward learning (Dölen et al., 2013; Hung et al., 2017), in this experiment we specifically targeted the NAc shell

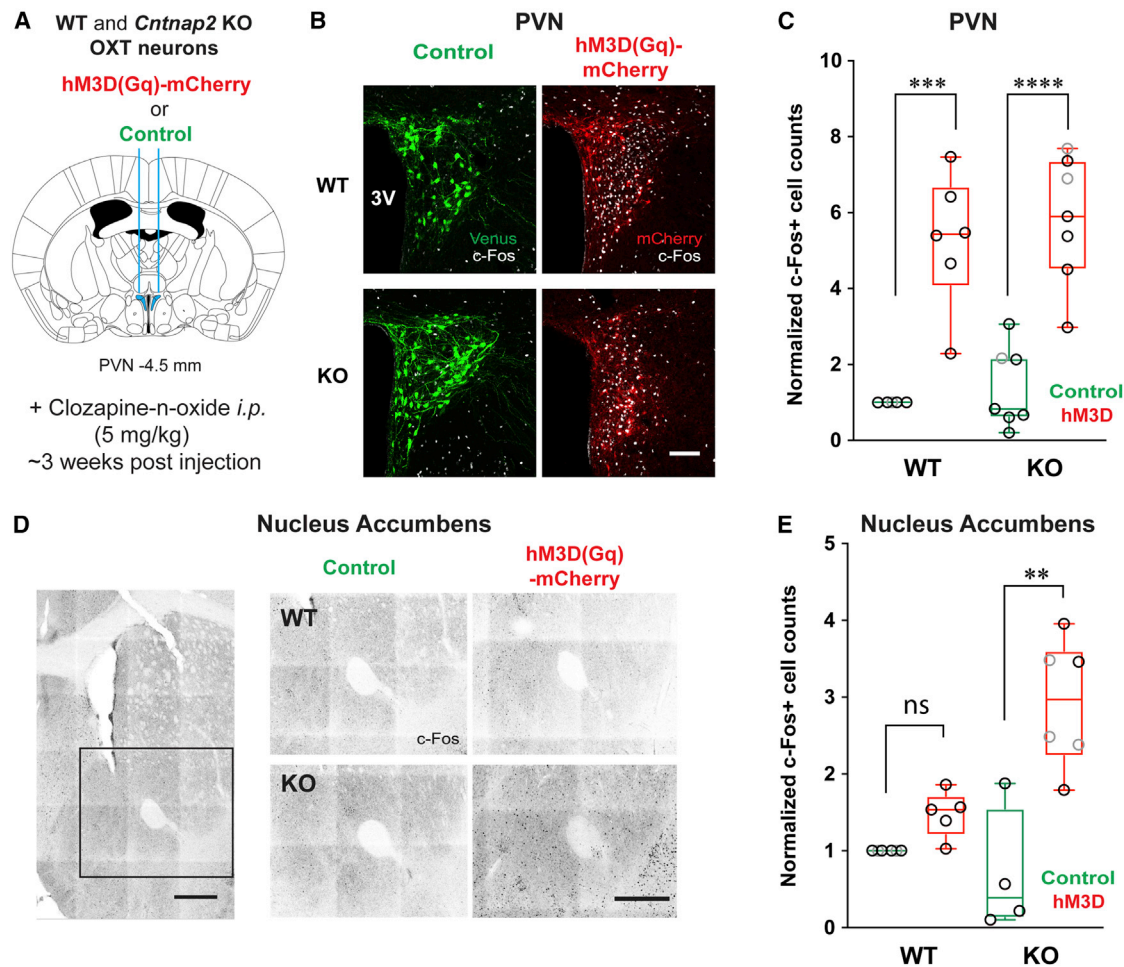


Figure 5. Chemogenetic activation of endogenous OXT release strongly activates the NAC

(A) A schematic of the DREADD approach used to activate endogenous OXT release.

(B) Confocal images displaying AAV-driven expression of fluorescent reporter proteins (Venus (control), green or hM3D(Gq)-mCherry, red) in PVN OXT neurons, overlaid with c-Fos immunostaining as a proxy for neuronal activation post clozapine-n-oxide (CNO) injection (white). 3V, 3rd ventricle. Scale bar, 100 μ m.

(C) Box-whisker plot (whiskers: min–max values, box: 25th–75th percentiles, circles: individual values, black for males and gray for females) compares the number of c-Fos+ cells in WT and KO PVN after hM3D or control virus injections. Circles represent individual datapoints (gray: females, black: males).

(D) Confocal images showing immunostained c-Fos+ cells in the NAC. Scale bar, 500 μ m.

(E) DREADD-stimulation of PVN OXT neurons significantly increases c-Fos+ cell counts in KO NAC, not WT. Kruskal-Wallis test. ** $p < 0.01$, *** $p < 0.005$, **** $p < 0.001$; ns, not significant.

(NACSh) area because of its heavy innervation with OXT fibers (Liao et al., 2020), the previously demonstrated excitatory response to OXT application *in vivo* (Moaddab et al., 2015), and the proposed role for it as a social hub region (Johnson et al., 2017). In a separate trial, each mouse received an equal amount of SAL infusion as control experiments. We found that KO mice spent a significantly longer amount of time investigating a novel, sex-matched juvenile mouse after receiving TGOT when compared to the SAL trials ($n = 10$ mice, $p = 0.04$; Figure 6B). These results demonstrate that OXTR activation in the NACSh is sufficient to increase social interaction in KO mice.

Finally, we asked whether the pro-social effects of OXT in KO mice could simply be replicated by triggering local endogenous OXT release within the NACSh. To test this, we used an

optogenetic strategy wherein expression of ChETA, a variant of Channelrhodopsin with fast time kinetics (Gunaydin et al., 2010), was targeted to PVN OXT neurons using a viral vector (Figure 6C). Histological examination of these mice confirmed robust expression of eYFP in the PVN and OXT fibers in the NACSh (Figure 6D), as well as proper targeting of the implanted cannulae (Figure 6B). ChETA and eYFP-control mice were tested with the home cage reciprocal social interaction assay, with or without blue light (457 nm) stimulation throughout the entire experimental period (10 min). We observed that light stimulation significantly increased the social behavior of KO-ChETA mice when compared to trials performed without light stimulation ($p = 0.03$; Figure 6E). We did not observe a similar effect in control KO mice ($p = 0.75$; Figure 6E), confirming that the behavioral change induced by blue light was driven by

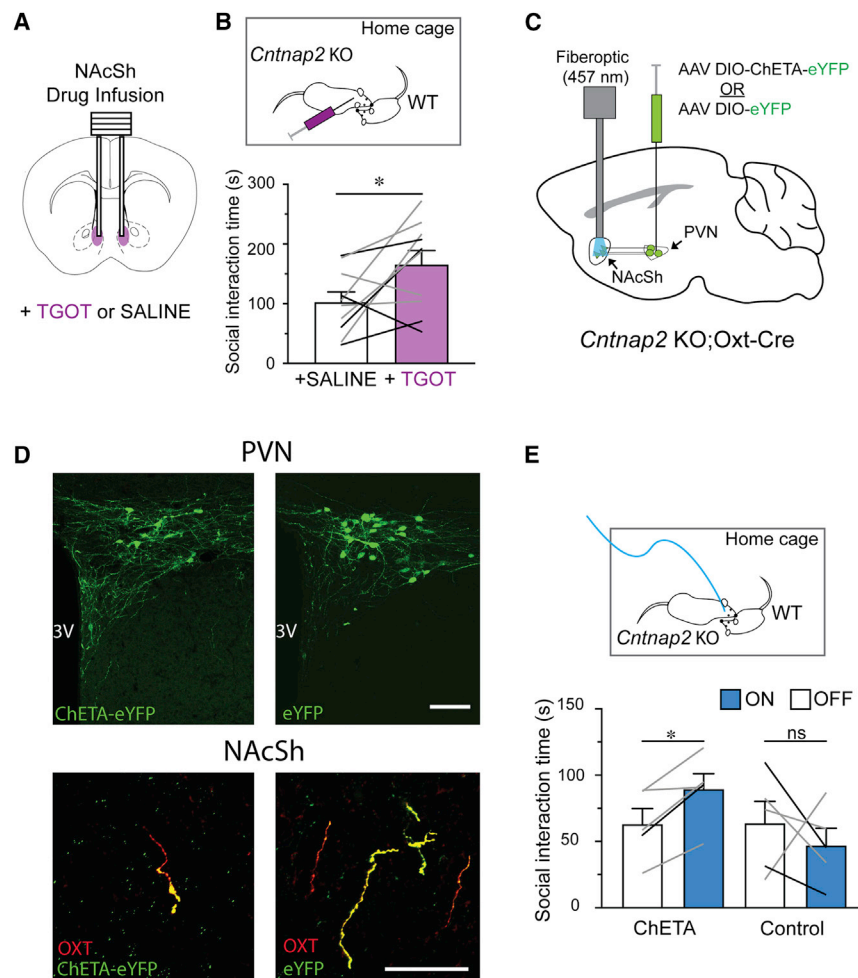


Figure 6. OXT in NAc increases social behavior in KO mice

(A) Schematic of *in vivo* NAcSh infusion. (B) Top: schematic of home cage social interaction assay combined with NAcSh infusion. Bottom: average social interaction time of KO mice with novel WT mice significantly increases after TGOT infusion. Paired t test. (C) Schematic illustrating *in vivo* optogenetic stimulation of NAcSh-targeted OXT release. (D) Confirmation of eYFP expression in the PVN and NAcSh of mice injected with AAVs packaging either ChETA-eYFP (left) or eYFP control (right). Scale bars, 100 μ m (top), 50 μ m (bottom). (E) Top: schematic of optogenetic stimulation during home cage reciprocal social interaction. Bottom: optogenetic stimulation significantly increases the average social interaction time of ChETA-expressing, but not control, KO mice. Lines represent individual animals (gray: females, black: males). One-way RM ANOVA, * $p < 0.05$; ns, not significant. Data are represented as mean \pm SEM.

optogenetic excitation of OXT neuron terminals. These two lines of independent evidence, pharmacological and optogenetic, establish that OXT signaling in the NAcSh serves as an important neuromodulator, likely mediating the pro-social effect of exogenous and endogenous OXT in KO mice.

DISCUSSION

A major hypothesis suggests that the behavioral symptoms of ASD are explained by aberrant rsFC, especially long-range disconnection that may occur as a result of developmental events (Geschwind and Levitt, 2007). Reflecting this hypothesis, and consistent with the human imaging data in subjects with idiopathic ASD (Cherkassky et al., 2006; Hull et al., 2017; Just et al., 2004; Kennedy and Courchesne, 2008; Starck et al., 2013), our rsfMRI results indicate the presence of abnormal basal rsFC in KO mice, such that core brain regions involved in social functions display a pattern of hypoconnectivity with each other and hyperconnectivity with other regions (Figure 1). In contrast, rsFC between brain regions whose major functions lie outside of the social domain (e.g., motor and sensory functions) do not show any genotype differences. Overwhelming patterns of hypo-

connectivity including the limbic and paralimbic system have been reported from the Autism Brain Imaging Data Exchange (ABIDE) study, which aimed to gain a consensus of the connectivity phenotype by aggregating a large number of ASD rsfMRI datasets (>1,000 subjects; Di Martino et al., 2014). Our findings of hypoconnectivity across many social brain regions, including limbic areas, in the KO mouse are remarkably similar to the findings of this well-powered clinical study in humans. The ABIDE study also found pat-

terns of hyperconnectivity involving subcortical areas, similar to our results (macroscale hyperconnectivity between FN-HPC, FN-THAL, and FN-MID). Therefore, the *Cntnap2* KO rsfMRI results presented here are surprisingly concordant with the rsFC patterns observed in the brains of individuals with ASD. These phenotypic similarities underscore the potential utility of some genetic mouse models for gaining a greater understanding of ASD neurobiology and development of translatable treatment options. At the same time, we recognize the heterogeneous etiology of ASD and do not suppose that this or any other single gene model is representative of the spectrum of this complex disorder.

Strikingly, administration of OXT normalized the network connectivity abnormalities in KO mice, increasing rsFC across social brain regions and decreasing it between these regions and other brain regions that were hyperconnected in KO mice without such treatment (Figure 1). This observation is also consistent with the previously proposed role of OXT in functionally coupling the nodes of social brain regions, facilitating social behavior (Johnson and Young, 2017). Interestingly, these effects were not observed in WT mice, revealing a unique mechanism by which OXT impacts the KO brain. It is important to note that the formulation of social or non-social brain regions is not absolute and is rather dependent

on the nature of the behaviors in question. Our categorization of social brain regions in this study is consistent with and based on previous literature defining networks of brain regions playing core roles in a wide range of social behavior, including the “mammalian social behavior network” (Newman, 1999), the “social decision-making network” (O’Connell and Hofmann, 2012), and the “social salience neural network” (Johnson et al., 2017).

The importance of the NAc in various types of social behavior is well documented across many species, including prairie voles (Aragona et al., 2003), mice (Dölen et al., 2013; Ko, 2017), rats (Ploeger et al., 1991), and humans (Floresco, 2015). We present several lines of experimental evidence that establish the NAc as an important region for the pro-social effects of OXT in *Cntnap2* KO mice (Peñagarikano et al., 2015), further supporting its role as a hub in the social reward network whose coordinated activity is critical for producing normal social behavior (Johnson and Young, 2017). First, our macroscale-level analysis identified the FN as the major brain structure exhibiting the highest number of aberrant connections in KO mice (Figure 1A). Second, OXT either partially or fully rescued these rsFC phenotypes (Figure 1D). Third, the NAc is the only FN area robustly activated by endogenous OXT (Figures 5D and 5E), highlighting its potential role as a substrate region for the pro-social effect of OXT in KO mice. Confirming this hypothesis, our behavioral experiments (Figure 6) demonstrate that either agonist activation of OXTR signaling in the NAcSh or optogenetically stimulating NAcSh-specific secretion of endogenous OXT sufficiently increases social behavior in KO mice. Importantly, the NAcSh has previously been identified as the integrative hub of the “social salience neural network” (Johnson et al., 2017). Our data are highly consistent with this model and further reveal that OXT signaling impairments within the NAc and the resulting functional uncoupling of the social brain may underlie social deficits caused by a loss of *Cntnap2*.

OXT is very weakly permeable through the blood-brain barrier (Ermisch et al., 1985), generating an ongoing debate as to whether and how peripherally administered OXT can affect brain activity (Leng and Ludwig, 2016; Quintana et al., 2018). Several possibilities exist. First, i.p. OXT may activate peripheral OXTRs, which in turn stimulates the activity of PVN OXT neurons through activation of a transynaptic circuit, such as the one involved in OXT-induced feeding regulation (Iwasaki et al., 2015) and OXT inhibition of methamphetamine addiction (Everett et al., 2021). Indeed, our pHMRI results show a robust increase (~8%) in the BOLD signal around the PVN in KO mice about 10 min after the injection, demonstrating rapid activation of the central OXT system (Figure 3). This central effect is long-lasting, with the BOLD signal elevation persisting throughout the scan duration (~40 min). Because the half-life of OXT is only a few minutes long (Ludwig and Leng, 2006), we hypothesize that PVN OXT neurons stimulate continued release of OXT onto downstream regions through the known positive feedback loop (Ludwig and Leng, 2006). Another possibility accounting for the KO-specific effect of OXT could be elevated OXTR expression at the sensory circumventricular organs, where there is increased access to circulating peptides due to higher permeability of the blood-brain barrier (Hosono et al., 1999). It may be possible that subfornical organ (SFO) neurons, once activated by the circulating OXT, excite PVN OXT neurons to stimulate endogenous release.

Lastly, there is also a possibility that the permeability of the blood-brain barrier in KO mice is increased, allowing a higher amount of OXT to get into the brain. Interestingly, Nr1-IV, the invertebrate ortholog of Caspr2 (the protein encoded by the *Cntnap2* gene), has previously been demonstrated to play a role in regulating a form of glia-glia contact important for maintaining septate junctions forming the *Drosophila* blood-brain barrier (Bellen et al., 1998). Because Caspr2 expression is thought to be associated with both neurons and glia in mice (Poliak et al., 1999), our observation raises the possibility that mutant mice may have a disrupted blood-brain barrier, a hypothesis that can be investigated in future studies.

In summary, we have uncovered the ability of OXT to robustly stimulate brain activity and reverse aberrant patterns of rsFC in a mouse model of ASD. Integration of multiple brain-wide datasets identifies the NAc as being a key region in this process, which we confirm with circuit-specific experimental approaches. These provocative findings reveal that mutations in a single ASD gene, *Cntnap2*, can drastically amplify and/or reverse the neuro-modulatory effects of OXT in specific brain regions, leading to behavioral modifications. Future studies aimed at identifying the molecular, cellular, and synaptic mechanisms that underlie the robust effects of OXT at the NAc will deepen our understanding of the link between *Cntnap2* and the central OXT system. Furthermore, identifying whether similar mechanisms also drive the social behavior phenotypes of other genetic models of ASD will be crucial for investigating whether our findings can be generalized for other ASD gene mutations. Interestingly, recent studies involving other genetic models of ASD also implicate OXT neurons in their social deficits (Harony-Nicolas et al., 2017; Hörnberg et al., 2020; Kitagawa et al., 2021; Lewis et al., 2020), supporting the emerging view that the OXT system may act as a convergence point connecting ASD gene mutations to social impairment.

STAR★METHODS

Detailed methods are provided in the online version of this paper and include the following:

- KEY RESOURCES TABLE
- RESOURCE AVAILABILITY
 - Lead contact
 - Materials availability
 - Data and code availability
- EXPERIMENTAL MODEL AND SUBJECT DETAILS
- METHOD DETAILS
 - Magnetic resonance imaging
 - OXT receptor autoradiography
 - iDISCO+ brain-wide imaging
 - Chemogenetic activation of endogenous OXT release
 - Home cage social interaction test
 - *In vivo* infusion of TGOT into the NAc shell
 - Optogenetic stimulation of OXT release in the NAcSh
- QUANTIFICATION AND STATISTICAL ANALYSIS
 - MRI analysis
 - Brain-wide analysis of c-Fos+ cell counts in iDISCO+ samples

- Region-specific analysis of c-Fos+ cell counts after OXT-DREADD activation
- Home cage social interaction test

SUPPLEMENTAL INFORMATION

Supplemental information can be found online at <https://doi.org/10.1016/j.neuron.2021.11.031>.

ACKNOWLEDGMENTS

D.H.G. and K.Y.C. were supported by the National Institute of Mental Health (NIMH; R01MH100027). D.H.G., N.G.H., and K.Y.C. were supported by the Simons Foundation Autism Research Initiative (Award 401457). K.Y.C. was supported by the NIMH (K99MH115143) and CIHR (Postdoctoral Fellowship). N.G.H. was supported by the National Institute of Neurological Disorders and Stroke (NINDS; R01NS091222) and the UCLA Brain Injury Research Center. L.A.D. was supported by NIH K01MH116264 and a NARSAD Young Investigator Award. R.A.I.B. was supported by the British Academy and Autism Research Trust. V.G. was supported by the German Research Foundation (DFG) grants GR 3619/15-1 and GR 3619/16-1 and the SFB Consortium 1158-2. O.P. was supported by MICINN (RTI2018-101427-B-I00). We thank Hal Gainer for the generous gift of anti-oxytocin antibody; Charles Bourque for helpful comments on the manuscript; Sophy Xiong, Jonathan Abrams, Qiuli Bi, and Andrew Frew for technical assistance; and members of the D.H.G. and P.G. laboratories for stimulating discussions and troubleshooting support.

AUTHOR CONTRIBUTIONS

D.H.G., K.Y.C., and N.G.H. conceived the study design. K.Y.C., M.S., E.S., and Y.L. collected fMRI data. K.Y.C., N.G.H., R.A.I.B., and E.S. analyzed fMRI data. K.Y.C., Y.L., and L.A.D. collected and analyzed c-Fos-iDISCO+ data. O.P. collected OXT receptor autoradiography data. K.Y.C., M.S., E.S., and H.D. collected and analyzed DREADD c-Fos data. V.G. provided the OXT promoter virus as well as consultation for its usage. K.Y.C., Y.L., and P.G. collected and analyzed OXT *in vivo* infusion and optogenetic data. K.Y.C. and D.H.G. wrote the initial drafts and prepared the manuscript and figures. R.A.I.B., V.G., P.G., L.A.D., O.P., and N.G.H. contributed to editing.

DECLARATION OF INTERESTS

The authors report no competing interests.

Received: March 8, 2020

Revised: September 3, 2021

Accepted: November 24, 2021

Published: December 20, 2021

REFERENCES

- Adamczak, J.M., Farr, T.D., Seehafer, J.U., Kalthoff, D., and Hoehn, M. (2010). High field BOLD response to forepaw stimulation in the mouse. *Neuroimage* 51, 704–712.
- Ahrens, E.T., and Dubowitz, D.J. (2001). Peripheral somatosensory fMRI in mouse at 11.7 T. *NMR Biomed.* 14, 318–324.
- Anderson, D.J. (2016). Circuit modules linking internal states and social behaviour in flies and mice. *Nat. Rev. Neurosci.* 17, 692–704.
- Aragona, B.J., Liu, Y., Curtis, J.T., Stephan, F.K., and Wang, Z. (2003). A critical role for nucleus accumbens dopamine in partner-preference formation in male prairie voles. *J. Neurosci.* 23, 3483–3490.
- Baio, J., Wiggins, L., Christensen, D.L., Maenner, M.J., Daniels, J., Warren, Z., Kurzius-Spencer, M., Zahorodny, W., Robinson Rosenberg, C., White, T., et al. (2018). Prevalence of Autism Spectrum Disorder Among Children Aged 8

- Years - Autism and Developmental Disabilities Monitoring Network, 11 Sites, United States, 2014. *MMWR Surveill. Summ* 67, 1–23.
- Barak, B., and Feng, G. (2016). Neurobiology of social behavior abnormalities in autism and Williams syndrome. *Nat. Neurosci.* 19, 647–655.
- Beckmann, C.F., and Smith, S.M. (2004). Probabilistic independent component analysis for functional magnetic resonance imaging. *IEEE Trans. Med. Imaging* 23, 137–152.
- Bellen, H.J., Lu, Y., Beckstead, R., and Bhat, M.A. (1998). Neurexin IV, caspr and paranodin—novel members of the neurexin family: encounters of axons and glia. *Trends Neurosci.* 21, 444–449.
- Ben-Barak, Y., Russell, J.T., Whitnall, M.H., Ozato, K., and Gainer, H. (1985). Neuropeptide Y in the hypothalamo-neurohypophyseal system. I. Production and characterization of monoclonal antibodies. *J. Neurosci.* 5, 81–97.
- Bernier, R., Golzio, C., Xiong, B., Stessman, H.A., Coe, B.P., Penn, O., Witherspoon, K., Gerdts, J., Baker, C., Vulto-van Silfhout, A.T., et al. (2014). Disruptive CHD8 mutations define a subtype of autism early in development. *Cell* 158, 263–276.
- Brumback, A.C., Ellwood, I.T., Kjaerby, C., Iafrati, J., Robinson, S., Lee, A.T., Patel, T., Nagaraj, S., Davatolhagh, F., and Sohal, V.S. (2018). Identifying specific prefrontal neurons that contribute to autism-associated abnormalities in physiology and social behavior. *Mol. Psychiatry* 23, 2078–2089.
- Chadman, K.K. (2014). Making progress in autism drug discovery. *Expert Opin. Drug Discov.* 9, 1389–1391.
- Chen, P., and Hong, W. (2018). Neural Circuit Mechanisms of Social Behavior. *Neuron* 98, 16–30.
- Cherkassky, V.L., Kana, R.K., Keller, T.A., and Just, M.A. (2006). Functional connectivity in a baseline resting-state network in autism. *Neuroreport* 17, 1687–1690.
- Cliethero, J.A., Reeck, C., Carter, R.M., Smith, D.V., and Huettel, S.A. (2011). Nucleus accumbens mediates relative motivation for rewards in the absence of choice. *Front. Hum. Neurosci.* 5, 87.
- de la Torre-Ubieta, L., Won, H., Stein, J.L., and Geschwind, D.H. (2016). Advancing the understanding of autism disease mechanisms through genetics. *Nat. Med.* 22, 345–361.
- DeNardo, L.A., Liu, C.D., Allen, W.E., Adams, E.L., Friedmann, D., Fu, L., Guenther, C.J., Tessier-Lavigne, M., and Luo, L. (2019). Temporal evolution of cortical ensembles promoting remote memory retrieval. *Nat. Neurosci.* 22, 460–469.
- Di Martino, A., Yan, C.G., Li, Q., Denio, E., Castellanos, F.X., Alaerts, K., Anderson, J.S., Assaf, M., Bookheimer, S.Y., Dapretto, M., et al. (2014). The autism brain imaging data exchange: towards a large-scale evaluation of the intrinsic brain architecture in autism. *Mol. Psychiatry* 19, 659–667.
- DiMario, F.J., Jr., Sahin, M., and Ebrahimi-Fakhari, D. (2015). Tuberous sclerosis complex. *Pediatr. Clin. North Am.* 62, 633–648.
- Dölen, G., Darvishzadeh, A., Huang, K.W., and Malenka, R.C. (2013). Social reward requires coordinated activity of nucleus accumbens oxytocin and serotonin. *Nature* 501, 179–184.
- Dorr, A.E., Lerch, J.P., Spring, S., Kabani, N., and Henkelman, R.M. (2008). High resolution three-dimensional brain atlas using an average magnetic resonance image of 40 adult C57Bl/6J mice. *Neuroimage* 42, 60–69.
- Eliava, M., Melchior, M., Knobloch-Bollmann, H.S., Wahis, J., da Silva Gouveia, M., Tang, Y., Ciobanu, A.C., Triana Del Rio, R., Roth, L.C., Althammer, F., et al. (2016). A New Population of Parvocellular Oxytocin Neurons Controlling Magnocellular Neuron Activity and Inflammatory Pain Processing. *Neuron* 89, 1291–1304.
- Ermisch, A., Barth, T., Rühle, H.J., Skopková, J., Hrbas, P., and Landgraf, R. (1985). On the blood-brain barrier to peptides: accumulation of labelled vasopressin, DesGlyNH₂-vasopressin and oxytocin by brain regions. *Endocrinol. Exp.* 19, 29–37.
- Everett, N.A., Turner, A.J., Costa, P.A., Baracz, S.J., and Cornish, J.L. (2021). The vagus nerve mediates the suppressing effects of peripherally administered oxytocin on methamphetamine self-administration and seeking in rats. *Neuropsychopharmacology* 46, 297–304.

- Fay, M.P., and Shaw, P.A. (2010). Exact and Asymptotic Weighted Logrank Tests for Interval Censored Data: The interval R package. *J. Stat. Softw.* 36, 1–34.
- Febo, M. (2011). Technical and conceptual considerations for performing and interpreting functional MRI studies in awake rats. *Front. Psychiatry* 2, 43.
- Feng, Z.-X., Dong, H., Qu, W.-M., and Zhang, W. (2018). Oral Delivered Dexmedetomidine Promotes and Consolidates Non-rapid Eye Movement Sleep via Sleep-Wake Regulation Systems in Mice. *Front. Pharmacol.* 9, 1196.
- Ferretti, V., Maltese, F., Contarini, G., Nigro, M., Bonavia, A., Huang, H., Gigliucci, V., Morelli, G., Scheggia, D., Manago, F., et al. (2019). Oxytocin Signaling in the Central Amygdala Modulates Emotion Discrimination in Mice. *Curr. Biol.* 29, 1938–1953.
- Fields, R.L., Ponzio, T.A., Kawasaki, M., and Gainer, H. (2012). Cell-type specific oxytocin gene expression from AAV delivered promoter deletion constructs into the rat supraoptic nucleus in vivo. *PLoS ONE* 7, e32085.
- Floresco, S.B. (2015). The nucleus accumbens: an interface between cognition, emotion, and action. *Annu. Rev. Psychol.* 66, 25–52.
- Friard, O., and Gamba, M. (2016). BORIS: a free, versatile open-source event-logging software for video/audio coding and live observations. *Methods Ecol. Evol.* 7, 1325–1330.
- Fukuda, M., Vazquez, A.L., Zong, X., and Kim, S.G. (2013). Effects of the α_2 -adrenergic receptor agonist dexmedetomidine on neural, vascular and BOLD fMRI responses in the somatosensory cortex. *Eur. J. Neurosci.* 37, 80–95.
- Galbusera, A., De Felice, A., Girardi, S., Bassetto, G., Maschietto, M., Nishimori, K., Chini, B., Papaleo, F., Vassanelli, S., and Gozzi, A. (2017). Intranasal Oxytocin and Vasopressin Modulate Divergent Brainwide Functional Substrates. *Neuropsychopharmacology* 42, 1420–1434.
- Gallo, F.T., Kathe, C., Morici, J.F., Medina, J.H., and Weisstaub, N.V. (2018). Immediate Early Genes, Memory and Psychiatric Disorders: Focus on c-Fos, Egr1 and Arc. *Front. Behav. Neurosci.* 12, 79.
- Geschwind, D.H., and Levitt, P. (2007). Autism spectrum disorders: developmental disconnection syndromes. *Curr. Opin. Neurobiol.* 17, 103–111.
- Ghosh, A., Michalon, A., Lindemann, L., Fontoura, P., and Santarelli, L. (2013). Drug discovery for autism spectrum disorder: challenges and opportunities. *Nat. Rev. Drug Discov.* 12, 777–790.
- Gigliucci, V., Leonzino, M., Busnelli, M., Luchetti, A., Palladino, V.S., D’Amato, F.R., and Chini, B. (2014). Region specific up-regulation of oxytocin receptors in the opioid opm1 (-/-) mouse model of autism. *Front. Pediatr.* 2, 91.
- Grandjean, J., Canella, C., Anckaerts, C., Ayranci, G., Bougacha, S., Bienert, T., Buehlmann, D., Coletta, L., Gallino, D., Gass, N., et al. (2020). Common functional networks in the mouse brain revealed by multi-centre resting-state fMRI analysis. *Neuroimage* 205, 116278.
- Grinevich, V., Knobloch, H.S., Roth, L.C., Althammer, F., Domansky, A., Vinnikov, I., Stanifer, M., and Boulant, S. (2016). Somatic transgenesis (Viral vectors). In *Masterclass in Neuroendocrinology Series: Molecular Neuroendocrinology: From Genome to Physiology*, First Edition, D. Murphy and H. Gainer, eds. (John Wiley & Sons, Ltd.), pp. 243–274.
- Grund, T., Tang, Y., Benusiglio, D., Althammer, F., Probst, S., Oppenländer, L., Neumann, I.D., and Grinevich, V. (2019). Chemogenetic activation of oxytocin neurons: Temporal dynamics, hormonal release, and behavioral consequences. *Psychoneuroendocrinology* 106, 77–84.
- Gunaydin, L.A., Yizhar, O., Berndt, A., Sohal, V.S., Deisseroth, K., and Hegemann, P. (2010). Ultrafast optogenetic control. *Nat. Neurosci.* 13, 387–392.
- Hablitz, L.M., Vinitsky, H.S., Sun, Q., Stæger, F.F., Sigurdsson, B., Mortensen, K.N., Lilius, T.O., and Nedergaard, M. (2019). Increased glymphatic influx is correlated with high EEG delta power and low heart rate in mice under anesthesia. *Science Advances* 5, eaav5447.
- Hagerman, R.J., Berry-Kravis, E., Hazlett, H.C., Bailey, D.B., Jr., Moine, H., Kooy, R.F., Tassone, F., Gantois, I., Sonenberg, N., Mandel, J.L., and Hagerman, P.J. (2017). Fragile X syndrome. *Nat. Rev. Dis. Primers* 3, 17065.
- Hahamy, A., Behrmann, M., and Malach, R. (2015). The idiosyncratic brain: distortion of spontaneous connectivity patterns in autism spectrum disorder. *Nat. Neurosci.* 18, 302–309.
- Hammock, E.A., and Levitt, P. (2013). Oxytocin receptor ligand binding in embryonic tissue and postnatal brain development of the C57BL/6J mouse. *Front. Behav. Neurosci.* 7, 195.
- Harony-Nicolas, H., Kay, M., du Hoffmann, J., Klein, M.E., Bozdagi-Gunal, O., Riad, M., Daskalakis, N.P., Sonar, S., Castillo, P.E., Hof, P.R., et al. (2017). Oxytocin improves behavioral and electrophysiological deficits in a novel Shank3-deficient rat. *eLife* 6, e18904.
- Hörnberg, H., Pérez-Garci, E., Schreiner, D., Hatstatt-Burklé, L., Magara, F., Baudouin, S., Matter, A., Nacro, K., Pecho-Vrieseling, E., and Scheiffele, P. (2020). Rescue of oxytocin response and social behaviour in a mouse model of autism. *Nature* 584, 252–256.
- Hosono, T., Schmid, H.A., Kanosue, K., and Simon, E. (1999). Neuronal actions of oxytocin on the subfornical organ of male rats. *Am. J. Physiol.* 276, E1004–E1008.
- Hull, J.V., Dokovna, L.B., Jacokes, Z.J., Torgerson, C.M., Irimia, A., and Van Horn, J.D. (2017). Resting-State Functional Connectivity in Autism Spectrum Disorders: A Review. *Front. Psychiatry* 7, 205.
- Hung, L.W., Neuner, S., Polepalli, J.S., Beier, K.T., Wright, M., Walsh, J.J., Lewis, E.M., Luo, L., Deisseroth, K., Dölen, G., and Malenka, R.C. (2017). Gating of social reward by oxytocin in the ventral tegmental area. *Science* 357, 1406–1411.
- Inenaga, K., and Yamashita, H. (1986). Excitation of neurones in the rat paraventricular nucleus in vitro by vasopressin and oxytocin. *J. Physiol.* 370, 165–180.
- Insel, T.R. (2010). The challenge of translation in social neuroscience: a review of oxytocin, vasopressin, and affiliative behavior. *Neuron* 65, 768–779.
- Insel, T.R., and Shapiro, L.E. (1992). Oxytocin receptor distribution reflects social organization in monogamous and polygamous voles. *Proc. Natl. Acad. Sci. USA* 89, 5981–5985.
- Iwasaki, Y., Maejima, Y., Suyama, S., Yoshida, M., Arai, T., Katsurada, K., Kumari, P., Nakabayashi, H., Kakei, M., and Yada, T. (2015). Peripheral oxytocin activates vagal afferent neurons to suppress feeding in normal and leptin-resistant mice: a route for ameliorating hyperphagia and obesity. *Am. J. Physiol. Regul. Integr. Comp. Physiol.* 308, R360–R369.
- Jeste, S.S., and Geschwind, D.H. (2014). Disentangling the heterogeneity of autism spectrum disorder through genetic findings. *Nat. Rev. Neurol.* 10, 74–81.
- Johnson, Z.V., and Young, L.J. (2017). Oxytocin and vasopressin neural networks: Implications for social behavioral diversity and translational neuroscience. *Neurosci. Biobehav. Rev.* 76 (Pt A), 87–98.
- Johnson, Z.V., Walum, H., Xiao, Y., Riefkohl, P.C., and Young, L.J. (2017). Oxytocin receptors modulate a social salience neural network in male prairie voles. *Horm. Behav.* 87, 16–24.
- Just, M.A., Cherkassky, V.L., Keller, T.A., and Minshew, N.J. (2004). Cortical activation and synchronization during sentence comprehension in high-functioning autism: evidence of underconnectivity. *Brain* 127, 1811–1821.
- Karayannis, T., Au, E., Patel, J.C., Pradhan, K., Mende, C., Taranda, J., Turaga, S.C., Arganda-Carreras, I., Ng, L., Hawrylycz, M.J., Rockland, K.S., et al. (2015). Mapping social behavior-induced brain activation at cellular resolution in the mouse. *Cell Rep.* 10, 292–305.
- King, J.B., Prigge, M.B.D., King, C.K., Morgan, J., Weathersby, F., Fox, J.C., Dean, D.C., 3rd, Freeman, A., Villaruz, J.A.M., Kane, K.L., et al. (2019). Generalizability and reproducibility of functional connectivity in autism. *Mol. Autism* 10, 27.

- Kitagawa, K., Matsumura, K., Baba, M., Kondo, M., Takemoto, T., Nagayasu, K., Ago, Y., Seiriki, K., Hayata-Takano, A., Kasai, A., et al. (2021). Intranasal oxytocin administration ameliorates social behavioral deficits in a *POGZ*^{WT/Q1038R} mouse model of autism spectrum disorder. *Mol. Brain* 14, 56.
- Knobloch, H.S., Charlet, A., Hoffmann, L.C., Eliava, M., Khrulev, S., Cetin, A.H., Osten, P., Schwarz, M.K., Seeburg, P.H., Stoop, R., and Grinevich, V. (2012). Evoked axonal oxytocin release in the central amygdala attenuates fear response. *Neuron* 73, 553–566.
- Ko, J. (2017). Neuroanatomical Substrates of Rodent Social Behavior: The Medial Prefrontal Cortex and Its Projection Patterns. *Front. Neural Circuits* 11, 41.
- Kogan, M.D., Vladutiu, C.J., Schieve, L.A., Ghandour, R.M., Blumberg, S.J., Zablotzky, B., Perrin, J.M., Shattuck, P., Kuhlthau, K.A., Harwood, R.L., and Lu, M.C. (2018). The Prevalence of Parent-Reported Autism Spectrum Disorder Among US Children. *Pediatrics* 142, e20174161.
- Kohls, G., Perino, M.T., Taylor, J.M., Madva, E.N., Cayless, S.J., Troiani, V., Price, E., Faja, S., Herrington, J.D., and Schultz, R.T. (2013). The nucleus accumbens is involved in both the pursuit of social reward and the avoidance of social punishment. *Neuropsychologia* 51, 2062–2069.
- Krashes, M.J., Koda, S., Ye, C., Rogan, S.C., Adams, A.C., Cusher, D.S., Maratos-Flier, E., Roth, B.L., and Lowell, B.B. (2011). Rapid, reversible activation of AgRP neurons drives feeding behavior in mice. *J. Clin. Invest.* 121, 1424–1428.
- Lau, W.K.W., Leung, M.-K., and Lau, B.W.M. (2019). Resting-state abnormalities in Autism Spectrum Disorders: A meta-analysis. *Sci. Rep.* 9, 3892.
- Lawrence, K.E., Hernandez, L.M., Bookheimer, S.Y., and Dapretto, M. (2019). Atypical longitudinal development of functional connectivity in adolescents with autism spectrum disorder. *Autism Res.* 12, 53–65.
- Lebow, M.A., and Chen, A. (2016). Overshadowed by the amygdala: the bed nucleus of the stria terminalis emerges as key to psychiatric disorders. *Mol. Psychiatry* 21, 450–463.
- Lein, E.S., Hawrylycz, M.J., Ao, N., Ayres, M., Bensinger, A., Bernard, A., Boe, A.F., Boguski, M.S., Brockway, K.S., Byrnes, E.J., et al. (2007). Genome-wide atlas of gene expression in the adult mouse brain. *Nature* 445, 168–176.
- Leng, G., and Ludwig, M. (2016). Intranasal Oxytocin: Myths and Delusions. *Biol. Psychiatry* 79, 243–250.
- Leslie, R.A., and James, M.F. (2000). Pharmacological magnetic resonance imaging: a new application for functional MRI. *Trends Pharmacol. Sci.* 21, 314–318.
- Levy, D.R., Tamir, T., Kaufman, M., Parabucki, A., Weissbrod, A., Schneidman, E., and Yizhar, O. (2019). Dynamics of social representation in the mouse prefrontal cortex. *Nat. Neurosci.* 22, 2013–2022.
- Lewis, E.M., Stein-O'Brien, G.L., Patino, A.V., Nardou, R., Grossman, C.D., Brown, M., Bangamwabo, B., Ndiaye, N., Giovino, D., Dardani, I., et al. (2020). Parallel Social Information Processing Circuits Are Differentially Impacted in Autism. *Neuron* 108, 659–675.e6.
- Liao, P.-Y., Chiu, Y.-M., Yu, J.-H., and Chen, S.-K. (2020). Mapping Central Projection of Oxytocin Neurons in Unmated Mice Using Cre and Alkaline Phosphatase Reporter. *Front. Neuroanat.* 14, 559402.
- Liska, A., Bertero, A., Gomolka, R., Sabbioni, M., Galbusera, A., Barsotti, N., Panzeri, S., Scattoni, M.L., Pasqualetti, M., and Gozzi, A. (2018). Homozygous Loss of Autism-Risk Gene *CNTNAP2* Results in Reduced Local and Long-Range Prefrontal Functional Connectivity. *Cerebral Cortex* 28, 1141–1153.
- Lowbridge, J., Manning, M., Haldar, J., and Sawyer, W.H. (1977). Synthesis and some pharmacological properties of [4-threonine, 7-glycine]oxytocin, [1-(L-2-hydroxy-3-mercaptopropanoic acid), 4-threonine, 7-glycine]oxytocin (hydroxy[Thr4, Gly7]oxytocin), and [7-Glycine]oxytocin, peptides with high oxytocic-antidiuretic selectivity. *J. Med. Chem.* 20, 120–123.
- Ludwig, M., and Leng, G. (2006). Dendritic peptide release and peptide-dependent behaviours. *Nat. Rev. Neurosci.* 7, 126–136.
- Lynch, C.J., Uddin, L.Q., Supekar, K., Khouzam, A., Phillips, J., and Menon, V. (2013). Default mode network in childhood autism: posteromedial cortex heterogeneity and relationship with social deficits. *Biol. Psychiatry* 74, 212–219.
- Magnuson, M.E., Thompson, G.J., Pan, W.J., and Keilholz, S.D. (2014). Time-dependent effects of isoflurane and dexmedetomidine on functional connectivity, spectral characteristics, and spatial distribution of spontaneous BOLD fluctuations. *NMR Biomed.* 27, 291–303.
- Marlin, B.J., Mitre, M., D'Amour, J.A., Chao, M.V., and Froemke, R.C. (2015). Oxytocin enables maternal behaviour by balancing cortical inhibition. *Nature* 520, 499–504.
- Menon, R., Grund, T., Zoicas, I., Althammer, F., Fiedler, D., Biermeier, V., Bosch, O.J., Hiraoka, Y., Nishimori, K., Eliava, M., et al. (2018). Oxytocin Signaling in the Lateral Septum Prevents Social Fear during Lactation. *Curr. Biol.* 28, 1066–1078.e1066.
- Meyer-Lindenberg, A., Domes, G., Kirsch, P., and Heinrichs, M. (2011). Oxytocin and vasopressin in the human brain: social neuropeptides for translational medicine. *Nat. Rev. Neurosci.* 12, 524–538.
- Mitre, M., Marlin, B.J., Schiavo, J.K., Morina, E., Norden, S.E., Hackett, T.A., Aoki, C.J., Chao, M.V., and Froemke, R.C. (2016). A Distributed Network for Social Cognition Enriched for Oxytocin Receptors. *J. Neurosci.* 36, 2517–2535.
- Mitre, M., Minder, J., Morina, E.X., Chao, M.V., and Froemke, R.C. (2018). Oxytocin Modulation of Neural Circuits. *Curr. Top. Behav. Neurosci.* 35, 31–53.
- Moaddab, M., Hyland, B.I., and Brown, C.H. (2015). Oxytocin excites nucleus accumbens shell neurons in vivo. *Mol. Cell. Neurosci.* 68, 323–330.
- Nakajima, M., Görlisch, A., and Heintz, N. (2014). Oxytocin modulates female sociosexual behavior through a specific class of prefrontal cortical interneurons. *Cell* 159, 295–305.
- Newman, S.W. (1999). The medial extended amygdala in male reproductive behavior. A node in the mammalian social behavior network. *Ann. N Y Acad. Sci.* 877, 242–257.
- O'Connell, L.A., and Hofmann, H.A. (2012). Evolution of a vertebrate social decision-making network. *Science* 336, 1154–1157.
- Oettl, L.L., Ravi, N., Schneider, M., Scheller, M.F., Schneider, P., Mitre, M., da Silva Gouveia, M., Froemke, R.C., Chao, M.V., Young, W.S., et al. (2016). Oxytocin Enhances Social Recognition by Modulating Cortical Control of Early Olfactory Processing. *Neuron* 90, 609–621.
- Oh, S.W., Harris, J.A., Ng, L., Winslow, B., Cain, N., Mihalas, S., Wang, Q., Lau, C., Kuan, L., Henry, A.M., et al. (2014). A mesoscale connectome of the mouse brain. *Nature* 508, 207–214.
- Owen, S.F., Tuncdemir, S.N., Bader, P.L., Tirko, N.N., Fishell, G., and Tsien, R.W. (2013). Oxytocin enhances hippocampal spike transmission by modulating fast-spiking interneurons. *Nature* 500, 458–462.
- Peñagarikano, O., Abrahams, B.S., Herman, E.I., Winden, K.D., Gdalyahu, A., Dong, H., Sonnenblick, L.I., Gruver, R., Almajano, J., Bragin, A., et al. (2011). Absence of *CNTNAP2* leads to epilepsy, neuronal migration abnormalities, and core autism-related deficits. *Cell* 147, 235–246.
- Peñagarikano, O., Lázaro, M.T., Lu, X.H., Gordon, A., Dong, H., Lam, H.A., Peles, E., Maidment, N.T., Murphy, N.P., Yang, X.W., et al. (2015). Exogenous and evoked oxytocin restores social behavior in the *Cntnap2* mouse model of autism. *Sci. Transl. Med.* 7, 271ra8.
- Ploeger, G.E., Willems, A.P., and Cools, A.R. (1991). Role of the nucleus accumbens in social memory in rats. *Brain Res. Bull.* 26, 23–27.
- Poliak, S., Gollan, L., Martinez, R., Custer, A., Einheber, S., Salzer, J.L., Trimmer, J.S., Shrager, P., and Peles, E. (1999). Caspr2, a new member of the neuroligin superfamily, is localized at the juxtaparanodes of myelinated axons and associates with K⁺ channels. *Neuron* 24, 1037–1047.
- Poliak, S., Salomon, D., Elhanany, H., Sabanay, H., Kiernan, B., Pevny, L., Stewart, C.L., Xu, X., Chiu, S.Y., Shrager, P., et al. (2003). Juxtaparanodal clustering of Shaker-like K⁺ channels in myelinated axons depends on Caspr2 and TAG-1. *J. Cell Biol.* 162, 1149–1160.

- Qin, J., Feng, M., Wang, C., Ye, Y., Wang, P.S., and Liu, C. (2009). Oxytocin receptor expressed on the smooth muscle mediates the excitatory effect of oxytocin on gastric motility in rats. *Neurogastroenterol. Motil.* **21**, 430–438.
- Quintana, D.S., Alvares, G.A., Hickie, I.B., and Guastella, A.J. (2015). Do delivery routes of intranasally administered oxytocin account for observed effects on social cognition and behavior? A two-level model. *Neurosci. Biobehav. Rev.* **49**, 182–192.
- Quintana, D.S., Smerud, K.T., Andreassen, O.A., and Djupesland, P.G. (2018). Evidence for intranasal oxytocin delivery to the brain: recent advances and future perspectives. *Ther. Deliv.* **9**, 515–525.
- Raichle, M.E. (2015). The brain's default mode network. *Annu. Rev. Neurosci.* **38**, 433–447.
- Renier, N., Adams, E.L., Kirst, C., Wu, Z., Azevedo, R., Kohl, J., Autry, A.E., Kadir, L., Umadevi Venkataraju, K., Zhou, Y., et al. (2016). Mapping of Brain Activity by Automated Volume Analysis of Immediate Early Genes. *Cell* **165**, 1789–1802.
- Riga, D., Matos, M.R., Glas, A., Smit, A.B., Spijker, S., and Van den Oever, M.C. (2014). Optogenetic dissection of medial prefrontal cortex circuitry. *Front. Syst. Neurosci.* **8**, 230.
- Ruzzo, E.K., Pérez-Cano, L., Jung, J.Y., Wang, L.K., Kashef-Haghighi, D., Hartl, C., Singh, C., Xu, J., Hoekstra, J.N., Leventhal, O., et al. (2019). Inherited and De Novo Genetic Risk for Autism Impacts Shared Networks. *Cell* **178**, 850–866.e26.
- Schindelin, J., Arganda-Carreras, I., Frise, E., Kaynig, V., Longair, M., Pietzsch, T., Preibisch, S., Rueden, C., Saalfeld, S., Schmid, B., et al. (2012). Fiji: an open-source platform for biological-image analysis. *Nat. Methods* **9**, 676–682.
- Scott, R., Sanchez-Aguilera, A., van Elst, K., Lim, L., Dehorter, N., Bae, S.E., Bartolini, G., Peles, E., Kas, M.J.H., Bruining, H., et al. (2019). Loss of *Cntnap2* Causes Axonal Excitability Deficits, Developmental Delay in Cortical Myelination, and Abnormal Stereotyped Motor Behavior. *Cerebral Cortex* **29**, 586–597.
- Scott-Van Zeeland, A.A., Dapretto, M., Ghahremani, D.G., Poldrack, R.A., and Bookheimer, S.Y. (2010). Reward processing in autism. *Autism Res.* **3**, 53–67.
- Selimbeyoglu, A., Kim, C.K., Inoue, M., Lee, S.Y., Hong, A.S.O., Kauvar, I., Ramakrishnan, C., Fenno, L.E., Davidson, T.J., Wright, M., et al. (2017). Modulation of prefrontal cortex excitation/inhibition balance rescues social behavior in *CNTNAP2*-deficient mice. *Science Translational Medicine* **9**, eaah6733.
- Smith, S.M., Jenkinson, M., Woolrich, M.W., Beckmann, C.F., Behrens, T.E., Johansen-Berg, H., Bannister, P.R., De Luca, M., Drobnjak, I., Flitney, D.E., et al. (2004). Advances in functional and structural MR image analysis and implementation as FSL. *Neuroimage* **23** (Suppl 1), S208–S219.
- Smith, S.M., Vidaurre, D., Beckmann, C.F., Glasser, M.F., Jenkinson, M., Miller, K.L., Nichols, T.E., Robinson, E.C., Salimi-Khorshidi, G., Woolrich, M.W., et al. (2013). Functional connectomics from resting-state fMRI. *Trends Cogn. Sci.* **17**, 666–682.
- Spreckelmeyer, K.N., Krach, S., Kohls, G., Rademacher, L., Irmak, A., Konrad, K., Kircher, T., and Gründer, G. (2009). Anticipation of monetary and social reward differently activates mesolimbic brain structures in men and women. *Soc. Cogn. Affect. Neurosci.* **4**, 158–165.
- Stafford, J.M., Jarrett, B.R., Miranda-Dominguez, O., Mills, B.D., Cain, N., Mihalas, S., Lahvis, G.P., Lattal, K.M., Mitchell, S.H., David, S.V., et al. (2014). Large-scale topology and the default mode network in the mouse connectome. *Proc. Natl. Acad. Sci. USA* **111**, 18745–18750.
- Stanley, D.A., and Adolphs, R. (2013). Toward a neural basis for social behavior. *Neuron* **80**, 816–826.
- Starck, T., Nikkinen, J., Rahko, J., Remes, J., Hurtig, T., Haapsamo, H., Jussila, K., Kuusikko-Gauffin, S., Mattila, M.L., Jansson-Verkasalo, E., et al. (2013). Resting state fMRI reveals a default mode dissociation between retrosplenial and medial prefrontal subnetworks in ASD despite motion scrubbing. *Front. Hum. Neurosci.* **7**, 802.
- Steinman, M.Q., Duque-Wilckens, N., and Trainor, B.C. (2019). Complementary Neural Circuits for Divergent Effects of Oxytocin: Social Approach Versus Social Anxiety. *Biol. Psychiatry* **85**, 792–801.
- Strauss, K.A., Puffenberger, E.G., Huentelman, M.J., Gottlieb, S., Dobrin, S.E., Parod, J.M., Stephan, D.A., and Morton, D.H. (2006). Recessive symptomatic focal epilepsy and mutant contactin-associated protein-like 2. *N. Engl. J. Med.* **354**, 1370–1377.
- Supekar, K., Kochalka, J., Schaer, M., Wakeman, H., Qin, S., Padmanabhan, A., and Menon, V. (2018). Deficits in mesolimbic reward pathway underlie social interaction impairments in children with autism. *Brain* **141**, 2795–2805.
- Takumi, T., Tamada, K., Hatanaka, F., Nakai, N., and Bolton, P.F. (2020). Behavioral neuroscience of autism. *Neurosci. Biobehav. Rev.* **110**, 60–76.
- Tang, Y., Benusiglio, D., Lefevre, A., Hilfiger, L., Althammer, F., Bludau, A., Hagiwara, D., Baudon, A., Darbon, P., Schimmer, J., et al. (2020). Social touch promotes interfemale communication via activation of parvocellular oxytocin neurons. *Nat. Neurosci.* **23**, 1125–1137.
- van Rooij, D., Anagnostou, E., Arango, C., Auzias, G., Behrmann, M., Busatto, G.F., Calderoni, S., Daly, E., Deruelle, C., Di Martino, A., et al. (2018). Cortical and Subcortical Brain Morphometry Differences Between Patients With Autism Spectrum Disorder and Healthy Individuals Across the Lifespan: Results From the ENIGMA ASD Working Group. *Am. J. Psychiatry* **175**, 359–369.
- Vanderschuren, L.J., Achterberg, E.J., and Trezza, V. (2016). The neurobiology of social play and its rewarding value in rats. *Neurosci. Biobehav. Rev.* **70**, 86–105.
- Walsh, J.J., Christoffel, D.J., Heifets, B.D., Ben-Dor, G.A., Selimbeyoglu, A., Hung, L.W., Deisseroth, K., and Malenka, R.C. (2018). 5-HT release in nucleus accumbens rescues social deficits in mouse autism model. *Nature* **560**, 589–594.
- Walum, H., and Young, L.J. (2018). The neural mechanisms and circuitry of the pair bond. *Nat. Rev. Neurosci.* **19**, 643–654.
- Wang, Q., Ding, S.-L., Li, Y., Royall, J., Feng, D., Lesnar, P., Graddis, N., Naeemi, M., Facer, B., Ho, A., et al. (2020). The Allen Mouse Brain Common Coordinate Framework: A 3D Reference Atlas. *Cell* **181**, 936–953.e20.
- Woolrich, M.W., Ripley, B.D., Brady, M., and Smith, S.M. (2001). Temporal autocorrelation in univariate linear modeling of FMRI data. *Neuroimage* **14**, 1370–1386.
- Woolrich, M.W., Behrens, T.E.J., Beckmann, C.F., Jenkinson, M., and Smith, S.M. (2004). Multilevel linear modelling for FMRI group analysis using Bayesian inference. *Neuroimage* **21**, 1732–1747.
- Wu, Z., Xu, Y., Zhu, Y., Sutton, A.K., Zhao, R., Lowell, B.B., Olson, D.P., and Tong, Q. (2012). An obligate role of oxytocin neurons in diet induced energy expenditure. *PLoS ONE* **7**, e45167.
- Yang, Y., and Wang, J.-Z. (2017). From Structure to Behavior in Basolateral Amygdala-Hippocampus Circuits. *Front. Neural Circuits* **11**, 86.

STAR★METHODS

KEY RESOURCES TABLE

REAGENT or RESOURCE	SOURCE	IDENTIFIER
Antibodies		
Rabbit anti-c-Fos	Synaptic Systems	Cat# 226 003; RRID: AB_2231974
Rabbit anti-c-Fos	Santa Cruz	Cat# sc-52; RRID: AB_2106783
Mouse anti-oxytocin (PS-38)	H. Gainer lab; Ben-Barak et al., 1985	RRID: AB_2315026
Goat anti-rabbit Alexa Fluor Plus 647	ThermoFisher	Cat#A32733; RRID: AB_2866492
Goat anti-mouse Alexa Fluor Plus 555	ThermoFisher	Cat#A32727; RRID: AB_2633276
Bacterial and virus strains		
AAV2-mOXT-hM3D(Gq)-mCherry-WPRE	Signagen with Plasmid from D. Geschwind lab; Peñagarikano et al., 2015	RRID: Addgene_70717
AAV2-hSyn-DIO-hM3D(Gq)-mCherry	Krashes et al., 2011	RRID: Addgene_44361
AAV2-mOXT-Venus	V. Grinevich lab; Knobloch et al., 2012	n/a
AAV2-hSyn-DIO-mCherry	Roth lab DREADDs (unpublished)	RRID: Addgene_50459
AAV1-Ef1a-DIO ChETA-EYFP	Gunaydin et al., 2010	RRID: Addgene_26968
AAV2-CAG-Flex-eGFP-WPRE	Oh et al., 2014	RRID: Addgene_51502
Chemicals, peptides, and recombinant proteins		
Oxytocin	Sigma-Aldrich	Cat#O3251
isopentane	Sigma-Aldrich	Cat#PHR1661
125I-OVT	PerkinElmer	Cat#NEX254
Trizma-HCl	Sigma-Aldrich	Cat#T5941
MgCl ₂	Sigma-Aldrich	Cat#M8266
PBS	Ambion	Cat#AM9624
Triton X-100	Sigma-Aldrich	Cat#X100-500mL
Tween-20	Sigma-Aldrich	Cat#P9416-100mL
DMSO	Fisher Scientific	Cat#D128-4
Sodium Azide	Sigma-Aldrich	Cat#58032-100G
Glycine	Sigma-Aldrich	Cat#G7126-500G
Heparin	Sigma-Aldrich	Cat#H3393-50KU
Hydrogen Peroxide (30%)	Sigma-Aldrich	Cat#216763-100ML
DiChloroMethane	Sigma-Aldrich	Cat#270997-12X100mL
DiBenzylEther	Sigma-Aldrich	Cat#108014-1KG
Paraformaldehyde (16%)	EMS	Cat#15710-S
Paraformaldehyde (32%)	EMS	Cat#15714
Sucrose	Sigma-Aldrich	Cat#S0389
Clozapine-n-oxide	Enzo Life Sciences	Cat#BML-NS105
Optimal Cutting Temperature (OCT) solution	TissueTech	Cat#4583
[Thr4,Gly7]-Oxytocin (TGOT)	Phoenix Pharmaceuticals	Cat#051-04
Evans Blue	Sigma-Aldrich	Cat#E2129
Agar	Fisher Scientific	Cat#BP9744500
Experimental models: Organisms/strains		
B6.129(Cg)- <i>Cntnap2</i> ^{tm1Pele} /J	E. Peles lab; Poliak et al., 2003	Cat#017482; RRID: IMSR_JAX:017482
B6;129S-Oxt ^{tm1.1(cre)Dolsn} /J	The Jackson Laboratory; Wu et al., 2012	Cat#024234; RRID: IMSR_JAX:024234
Software and algorithms		
Prism 9	GraphPad	https://www.graphpad.com/scientific-software/prism/

(Continued on next page)

Continued

REAGENT or RESOURCE	SOURCE	IDENTIFIER
Python 2.7	Python Software Foundation	https://www.python.org/
Zen Software	Zeiss Microscope	https://www.zeiss.com/microscopy/int/products/microscope-software/zen.html
Adobe Illustrator	Adobe	https://www.adobe.com/ca/products/illustrator.html
MATLAB 2018b	Mathworks	https://www.mathworks.com/products/matlab.html
ClearMap	Renier et al., 2016	https://idisco.info/clearmap-2/
Paravision 5.2	Bruker	https://www.bruker.com/en/products-and-solutions/preclinical-imaging/paravision-360.html
FSL Tools	FSL	https://fsl.fmrib.ox.ac.uk/fsl/
Perm package in R	Fay and Shaw, 2010	https://CRAN.R-project.org/package=perm
BORIS	Friard and Gamba, 2016	https://www.boris.unito.it/
FIJI	Schindelin et al., 2012	https://imagej.net/software/fiji/

RESOURCE AVAILABILITY

Lead contact

Further information and requests for resources and reagents should be directed to and will be fulfilled by the Lead Contact, Daniel H. Geschwind (dhg@mednet.ucla.edu).

Materials availability

This paper does not report original materials.

Data and code availability

- All data reported in this paper will be shared by the lead contact upon request.
- This paper does not report original code.
- Any additional information required to reanalyze the data reported in this paper is available from the lead contact upon request.

EXPERIMENTAL MODEL AND SUBJECT DETAILS

Mutant mice lacking the *Cntnap2* gene (Caspr2-null mice or *Cntnap2*^{-/-}) were obtained from Dr. Elior Peles ([Poliak et al., 2003](#)) and backcrossed to the C57BL/6J background for over 12 generations. Experimental *Cntnap2* mutant and WT mice were obtained from heterozygous crossings and used for experiments when they reached adulthood (8 weeks or older). Both sexes were used as experimental animals – they were randomly assigned to groups and no obvious differences were noted. The three obtained genotypes were housed together with three to four same sex mice per cage. A subset of experimental mice were obtained from crossing male breeder mice that are heterozygous for *Cntnap2* KO and homozygous Oxt-Cre (obtained from JAX, #024234) with female heterozygous *Cntnap2* KO mice to produce offspring experimental mice that are homozygous for *Cntnap2* KO and heterozygous for Oxt-Cre (*Cntnap2*^{-/-};Oxt^{Cre/+}). All mice were kept in 12 h light/12 h dark cycle and had ad-lib access to food and water. All procedures involving animals were performed in accordance with the UCLA Animal Research Committee, and the NIH Guide for the Care and Use of Laboratory Animals.

METHOD DETAILS

Magnetic resonance imaging

The mouse to be scanned was first briefly anesthetized with 2% isoflurane vaporized in oxygen flowing at 1 L/min, then placed on an MRI-compatible cradle. A single-channel surface coil (Bruker) was placed over the head of the mouse. For resting-state scans, a 3 mm-thick agar gel cap (Sigma, 3% in distilled water) was placed between the head and the surface coil, in order to reduce signal distortion in the blood-oxygen-level-dependent (BOLD) signal ([Adamczak et al., 2010](#)). To minimize time-dependent effects of the anesthetic on the BOLD signal, these initial steps were performed within a 10–15-min time window ([Magnuson et al., 2014](#)). Isoflurane was gradually discontinued and sedation was initiated with a single subcutaneous (s.c.) injection of dexmedetomidine (Dexdomitor®),

Zoetis; 0.15 mg/kg) followed by continuous s.c. infusion at 0.3 mg/kg/h throughout the duration of the imaging as described in a previous publication (Adamczak et al., 2010). Respiration and body temperature of the mouse were continuously monitored remotely, and maintained in a physiological range ($37 \pm 1^\circ\text{C}$; Small Animal Instruments Inc.) by a homeothermically-controlled forced warm air over the body (SA11 Instr, Inc., USA). At the end of the imaging session, sedation was reversed by atipamezole (Antisedan®, Pfizer) at 1.5 mg/kg (i.p.). Magnetic resonance imaging was performed using a 7 Tesla (T) Biospec small animal MRI system using Paravision 5.2 software (Bruker). Data were acquired using the S116 Bruker gradients (400 mT/m) in combination with a single-channel surface coil (described above) and a 72 mm birdcage transmit coil. An initial series of scans was performed to confirm proper head position, then localized FASTMAP shimming was performed to improve field homogeneity.

Pharmacological MRI

T2-weighted structural scans were acquired with a Rapid-Relaxation-with-Enhancement (RARE) sequence (RARE factor = 8, Echo time (TE) = 56 ms, repetition time (TR) = 6,018 ms, 4 averages, field-of-view (FOV) = 1.8×1.2 cm, slice thickness = 0.5 mm, 18 slices, FA = 90 deg, bandwidth (BW) = 50 kHz, matrix = 60×40). Then, 45-min long functional (BOLD) data were acquired using the same image geometry as the structural scans, with a one-shot, interleaved, gradient-echo echo planar imaging sequence with the following parameters: TE = 16 ms, TR = 2,000 ms, FA = 70 degrees, BW 400 kHz and a data matrix of 60×40 . 10 dummy scans were used to allow the T1 signal to reach steady-state prior to signal acquisition. OXT (Sigma, 1 mg/kg i.p. at 1 mg/mL) or saline was administered following 5 min of baseline imaging data collection, after which imaging data was acquired in a continuous manner for the next 40 min.

Resting-state MRI

Structural and functional data were acquired using above-described parameters, with the following modifications: field-of-view (FOV) = 3.0×3.0 cm, matrix = 128×64 ; functional (BOLD) scans acquired using a two-shot gradient-echo echo-planar imaging (GE-EPI) sequence, TE = 19 ms, TR = 1,000 ms (2,000 ms per volume), FA = 70 degrees, BW 400 kHz and a data matrix of 128×64 , Fourier transformed to 128×128 , voxel resolution $0.23 \times 0.23 \times 0.5$ mm. For each mouse, one 5-min resting-state scan (150 volumes) was acquired at the baseline, and then OXT (Sigma, 1 mg/kg i.p. at 1 mg/mL) or saline of the same volume was administered via a catheter placed prior to scanning. 5-min resting-state scans were acquired every 10 min, during the 40-min period following OXT/saline administration.

OXT receptor autoradiography

Following anesthesia and decapitation, brains were quickly removed and frozen in -70°C isopentane, and stored at -80°C . Sets of coronal brain sections ($20 \mu\text{m}$) were cut in a cryostat and thawmounted on Superfrost plus slides (stored at -80°C until processing for autoradiography). Autoradiography was performed using 40 pM concentration of OXT receptor ligand, 125I-ornithine vasotocin (OVT; PerkinElmer, NEX254) following standard protocols (Ferretti et al., 2019; Menon et al., 2018). Briefly, sections were thawed at room temperature, and fixed in 0.1% paraformaldehyde. After wash in 50 mM Tris-HCl (pH 7.4), the sections were incubated in 50pM 125I-labeled ligand in 50 mM Tris, 10 mM MgCl_2 , 0.1% bovine serum albumin (BSA), and 0.05% bacitracin. Excess ligand was removed by washing in 50 mM Tris-HCl (pH 7.4) / 10 mM, then in 50 mM Tris-HCl (pH 7.4) / 10 mM MgCl_2 . Finally, the sections were air-dried and exposed to Kodak BioMax MR film. Receptor binding patterns were qualitatively assessed.

iDISCO+ brain-wide imaging

Sample processing and imaging

Animals were single housed for 2 h prior to OXT administration (Sigma, 1 mg/kg i.p.). They were returned to their single-housed cages immediately after injection. 2 h after injection, they were perfused transcardially with PBS followed by 4% PFA in PBS. Brains were extracted and postfixed overnight at 4°C . The brains were then divided into two halves by cutting in the sagittal plane, then processed with the iDISCO+ immunolabeling, following a previously described protocol (Renier et al., 2016). Samples were stained with c-Fos primary antibody (Synaptic Systems 226 003, 1:500), then Alexafluor 647 secondary antibody (ThermoFisher Scientific, 1:500). At least one day after clearing, iDISCO+ samples were imaged on a light-sheet microscope (Ultramicroscope II, LaVision Biotec) equipped with a sCMOS camera (Andor Neo) and a $2\text{A}\sim/0.5$ NA objective lens (MVPLAPO $2\text{A}\sim$) using 488-nm and 640-nm lasers. The samples were scanned at 1.6x magnification with a z-thickness of $3 \mu\text{m}$ using the continuous light-sheet scanning method with the dynamic horizontal focus for the 640-nm channel (20 acquisitions per plane), and without horizontal scanning for the 488-nm autofluorescence. Modifications and continuous updates to the iDISCO+ protocol can be found at <http://www.idisco.info>.

Chemogenetic activation of endogenous OXT release

Bilateral stereotaxic injections of 500 nL of AAV2-mOXT-hM3D(Gq)-mCherry-WPRE (custom generated from Signagen with plasmid from D. Geschwind laboratory (Peñagarikano et al., 2015), or AAV2-hSyn-DIO-hM3D(Gq)-mCherry (Krashes et al., 2011) were performed into the PVN of the hypothalamus in WT and KO mice according to the following coordinates from Bregma: antero-posterior -0.60 mm; dorso-ventral -4.80 mm; lateral ± 0.20 mm. Another group of WT and KO mice received injections of AAV2-mOXT-Venus (V. Grinevich laboratory, Germany; Grinevich et al., 2016; Knobloch et al., 2012) or AAV2-hSyn-DIO-mCherry (Krashes et al., 2011) to control for the effects of surgeries and CNO administration. Mice that received equal volume injections of the viruses containing the Double-Floxed Inverted Open reading frame (DIO) were also heterozygous for the Oxt-Cre transgene (Oxt^{Cre/+}). Injections were performed at a rate of 100 nL/min with a glass micropipette ($50 \mu\text{m}$ tip diameter) using a Nanoliter 2000 microinjection system (WPI) attached to a Micro4 pump (WPI).

Three weeks after stereotaxic viral injections, WT and KO mice were singly housed and given clozapine-n-oxide (Enzo Life Sciences, 5 mg/kg, i.p.) after a habituation period of at least 1 h. 2 h after injection, mice were deeply anesthetized with 4% isoflurane and intracardially perfused with 4% paraformaldehyde in 0.1M PBS (freshly diluted from 16 or 32% stock, Electron Microscopy Sciences). Brains were subsequently removed and incubated in 0.1 M phosphate-buffered solution containing 30% sucrose at 4°C for 2–3 days. Brains were then embedded in optimal cutting temperature solution (TissueTech) at –80°C, and cryosectioned at 50 μ m thickness. Sections were stained with rabbit polyclonal anti-c-Fos antibody (1:500, Santa Cruz, sc-52) and goat anti-rabbit Alexa 647 secondary antibody (1:500). Confocal images were obtained at 10x magnification using a Zeiss 880 laser-scanning confocal microscope and analyzed using ImageJ (NIH).

Home cage social interaction test

Home cage social interaction assay of adult KO mice was performed adapting a previously used juvenile social play protocol (Peñagarikano et al., 2015). Briefly, adult KO mice and another group of juvenile (3–5 weeks old) WT mice, serving as novel social stimuli, were each singly housed in a new complete cage set up. They were then allowed to habituate for at least 1 h in a dark room with white noise. Immediately prior to the social interaction assay, each pair of sex-matched, juvenile-adult pair separately underwent another phase of 10-min solitary home cage exploration period in new home cages without lids. The pair was then placed together into another new home cage with no lid, meeting each other for the first time. They were allowed to freely interact for 10 min.

In vivo infusion of TGOT into the NAc shell

Adult KO mice were implanted with bilateral guide cannulae (Plastics One; 26G, 1.0 mm spacing, 3.5 mm long) targeting the NAcSh using the following stereotaxic coordinates from Bregma: antero-posterior +1.3 mm; dorso-ventral –3.5 mm; lateral \pm 0.5 mm. After at least 4 days of recovery, experimental mice were subjected to home cage social interaction tests described as above. Prior to the 10-min solitary home cage exploration period, TGOT (0.25 μ L/side for a total of 0.5 μ L/mouse, dissolved at 14 ng/ μ L in 0.9% saline; Phoenix Pharmaceuticals) or an equivalent volume of saline was delivered to each side of the NAcSh for a total of 0.5 μ L injection volume per mouse. Infusion was delivered at a rate of 0.1 μ L/min via a bilateral internal cannula (Plastics One; 33G, 1.0 mm spacing, 4.5 mm long). The internal cannula was left in place for 2.5 min after injection to allow for diffusion into the surrounding brain tissue. Each mouse underwent both TGOT and saline infusion trials separated by at least 1 day, the order of which were counterbalanced within the experimental group. After the conclusion of behavior experiments, mice were injected with a small volume (\sim 0.1 μ L) of 1% Evans blue (Sigma; diluted to 1% in 0.9% saline) through the internal cannula for visualization of injection sites, then perfused with paraformaldehyde solution (4% in PBS, Wako Chemicals). The brains were extracted, vibratome-sectioned and imaged on a confocal microscope (LSM 900, Zeiss) to confirm cannula placement.

Optogenetic stimulation of OXT release in the NAcSh

Adult KO mice were stereotaxically injected AAV1-Ef1a-DIO ChETA-EYFP (500 nL/side; Addgene #26968; Gunaydin et al., 2010) into the PVN of the hypothalamus as described above. Another group of KO mice were injected with or AAV2-CAG-Flex-eGFP-WPRE (Addgene #51502; Oh et al., 2014) or AAV2-mOXT-Venus (generated by V. Grinevich laboratory, Germany; Grinevich et al., 2016; Knobloch et al., 2012) to serve as controls. Following viral injections, dual-core optic cannula (200 μ m core, 700 μ m spacing, 0.39 NA, Thorlabs) was implanted into the NAcSh of each mouse using the following stereotaxic coordinates from Bregma: antero-posterior +1.3 mm; dorso-ventral –3.5 mm; lateral \pm 0.35 mm. The cannulae were fixed to the skull of mice using Metabond (Parkell).

After at least 3 weeks have passed, home cage social interaction assay (described above) was performed with or without optogenetic stimulation in separate trials. A patch cord was connected to the implanted mice immediately prior to the 10-min habituation stage in the cage without the lid. During optogenetic stimulation trials, mice received light stimulation (473 nm DPSS laser at 30 Hz, 10 ms width) at \sim 30 mW laser intensity measured from the tip of each dual-core cannula (\sim 15 mW estimated laser intensity from each core) throughout the entire free social interaction period. Trials were separated by at least 1 day, and the order of the two trials were counterbalanced. After the conclusion of behavior experiments, mice were perfused with paraformaldehyde solution (4% in PBS, Wako Chemicals). The brains were extracted, vibratome-sectioned and imaged on a confocal microscope (LSM 900, Zeiss) to confirm cannula placement and PVN-specific expression of eYFP, eGFP, or Venus. A subset of sections were stained with PS38 mouse monoclonal anti-oxytocin antibody (1:500, a gift of H. Gainer; Ben-Barak et al., 1985) and goat anti-mouse Alexa 555 secondary antibody (1:500; Thermofisher) to confirm cellular identity.

QUANTIFICATION AND STATISTICAL ANALYSIS

Each n represents the number of animals. N values for each experimental dataset are listed in the figure legends. Summary data are either represented as box-whisker plots (whisker: min-max values, box: 25–75th percentile) or bar plots (mean \pm SEM) with individual values. Kolmogorov-Smirnov test was performed to check for normality of datasets prior to conducting t test or ANOVA. The details of each analysis method and statistical test used are listed below.

MRI analysis

Analysis was performed using FSL tools (Smith et al., 2004; see Figure S1B for an illustration of the analysis pipeline). The following pre-analysis corrections were performed: BET brain extraction, MCFLIRT motion correction, slice timing correction, and smoothing at 5 mm. Scans with a large magnitude of head movement were identified and excluded from further analysis. Using FLIRT, all structural scans were co-registered to a single structural scan selected as a reference. The same transformation matrix was then applied to functional (BOLD) scans.

For Atlas-based analyses, regions-of-Interest (ROIs) were defined using a parcellated *in vivo* mouse brain atlas custom-constructed from the Allen brain histological atlas (Lein et al., 2007) co-registered to Dorr 3D mouse brain atlas (Dorr et al., 2008). The parcellated atlas was co-registered to each functional scan. 46 brain ROIs were defined intra- and inter-hemispherically: OLF, olfactory cortex, ORB, orbital area, ACC, anterior cingulate cortex, ASA, association areas, AUD, auditory cortex, INS, insular cortex, LIM, limbic cortex, MO, motor cortex, SS, somatosensory cortex, PIR, piriform cortex, RSA, retrosplenial area, DP, dorsal peduncular cortex, NAC, nucleus accumbens, LS, lateral septum, HPC, hippocampal area, BNST, bed nucleus of stria terminalis, CP, caudoputamen, LH, lateral hypothalamus, TH, thalamus, PAL, pallidum, MH, medial hypothalamus, MS, medial septum, MID, midbrain, PVN, paraventricular nucleus of the hypothalamus, RN, reticular nucleus, VTA, ventral tegmental area (L, left, R, right). Grouping of major brain structures (CTX, HPC, MID, THAL, HYPO, FN, OLF) followed the annotation rules of the Allen Brain Atlas (Lein et al., 2007; Wang et al., 2020). Classification of “social” (OLF, ORB, ACC, INS, LIM, PIR, DP, NAC, LS, BNST, LH, MH, MS, and PVN) and “other” regions (the rest of ROIs) was performed based on established roles evident in existing literature (e.g., Anderson, 2016; Chen and Hong, 2018; Kim et al., 2015).

Pharmacological MRI

Statistically significant BOLD activation associated with OXT or saline administration was first identified at the single-subject level using general linear modeling (GLM; cluster thresholds: $z < 1.7$, $p < 0.05$; multiple-comparison corrected) in FSL’s FEAT tool (Woolrich et al., 2001). Then, group-level comparisons were made between OXT and saline administered mice for each genotype using a t test (cluster thresholds: $z < 1.7$, $p < 0.001$; Woolrich et al., 2004). To assess Δ BOLD post OXT administration, the average BOLD time course from each ROI defined by the 46-region parcellated atlas was extracted and baseline-subtracted, then values from the last 150 volumes were averaged. Values for OXTR expression were obtained by averaging male and virgin female percentage of OXTR-expressing DAPI-positive cells for each ROI (Mitre et al., 2016). Values for OXT fiber density were obtained by assigning numerical values to previously reported regional fiber intensity ratings (Liao et al., 2020) as follows: - (0), \pm (1), + (2), ++ (3), +++ (4), ++++ (5), +++++ (6). Sub-regional values were averaged. Regression analysis was performed using Prism 9 (GraphPad). p values below 0.05 were considered to be statistically significant.

Resting-state MRI

Pairwise-ROI Analysis. For atlas-based ROI analysis, the average BOLD time course from each ROI defined by the 46-region parcellated atlas was extracted. rsFC between ROI pairs was computed using Pearson’s correlation analysis, and then Fisher’s z transformation was applied using MATLAB R2018b (Mathworks). Statistical differences between experimental groups were tested using Monte Carlo permutation tests using the perm package in R (10,000 repetitions; Fay and Shaw, 2010; <https://CRAN.R-project.org/package=perm>) for comparisons between major brain structure groupings and “social vs. other” comparisons. t test function in MATLAB was used to assess statistical significance for individual pairwise-ROI comparisons. p values below 0.05 were considered to be statistically significant.

For independent component (IC)-based ROI analysis, group-ICA was performed on all functional scans to identify 40 ICs followed by a dual regression to back-project spatial maps and time series for individual scans using FSL’s MELODIC and dual regression tools (Beckmann and Smith, 2004). Correlation matrices were made for all 40 component pairs to assess between-component connectivity. Paired t tests, corrected at FDR = 0.1, were performed within each genotype group to test the effect of OXT on between-component correlations.

Brain-wide analysis of c-Fos+ cell counts in iDISCO+ samples

Cell counts were calculated blind to experimental conditions. Images from iDISCO+ samples immunostained for Fos+ cells were quantified using the ClearMap cell detection module (Renier et al., 2016), with cell detection parameters optimized and validated by expert users based on the intensity and shape parameters of Fos immunolabeling profile (specific values available upon request). The image stack of autofluorescence in the 488 nm channel was aligned to the Allen Institute’s Common Coordinate Framework (CCF; Wang et al., 2020) using the Elastix toolbox and subsequently, the corresponding 640 nm channel image stack was transformed to the same coordinates. Statistical comparisons at the voxel level were performed using an unpaired t test within ClearMap. To generate region-based quantification, CCF parcellations collapsed into ~ 100 regions were applied to the whole brain quantification data. Regional values were then statistically compared with Kruskal-Wallis test with Dunn’s multiple comparison test using Prism 9 (GraphPad). Regression analysis comparing fMRI and iDISCO data was performed using Prism 9. p values below 0.05 were considered to be statistically significant.

Region-specific analysis of c-Fos+ cell counts after OXT-DREADD activation

Outlines over each brain region were drawn with references to The Allen Mouse Brain Atlas (Lein et al., 2007; Allen Institute, <http://mouse.brain-map.org/>) then the number of c-Fos+ cells was quantified by a blinded experimenter using the Analyze Particles tool in

Fiji (Schindelin et al., 2012). Counts for each section were normalized to the size of selected area, except for the PVN where raw counts were used for comparisons. Statistical comparisons were performed using One-way ANOVA with Tukey's multiple comparisons test or Kruskal-Wallis test with Dunn's multiple comparison test with Prism 9 (Graphpad), where p values of below 0.05 were considered as statistically significant.

Home cage social interaction test

Video-recordings of home cage reciprocal social interaction tests were manually analyzed by a blinded observer. Each social interaction event (i.e., sniffing or touching) was logged using BORIS (Friard and Gamba, 2016). Although rarely observed, pairs of mice displaying excessive aggressive behavior were excluded from the final dataset. Statistical comparison of behavioral datasets was performed using Prism (paired t test or RM ANOVA as appropriate). p values below 0.05 were considered as statistically significant.